A spline-based non-linear diffeomorphism for multimodal prostate registration

Jhimli Mitra [a,b,*], Zoltan Kato [c], Robert Martí [b], Arnau Oliver [b], Xavier Lladó [b], Désiré Sidibé [a], Soumya Ghose [a,b], Joan C. Vilanova [d], Josep Comet [e], Fabrice Meriaudeau [a]

[a] Le2i-UMR CNRS 6306, Université de Bourgogne, 12 rue de la Fonderie, 71200 Le Creusot, France
[b] Computer Vision and Robotics Group, Universitat de Girona, Campus Montilivi, Edifici PIV, s/n, 17071 Girona, Spain
[c] Dept. of Image Processing and Computer Graphics, University of Szeged, H-6701 Szeged, P.O. Box 652, Hungary
[d] Girona Magnetic Resonance Center, 26 Carrer Joan Maragall, 17002 Girona, Spain
[e] Hospital Dr. Josep Trueta, Av. França, s/n, 17007 Girona, Spain

ARTICLE INFO

ABSTRACT

This paper presents a novel method for non-rigid registration of transrectal ultrasound and magnetic resonance prostate images based on a non-linear regularized framework of point correspondences obtained from a statistical measure of shape-contexts. The segmented prostate shapes are represented by shape-contexts and the Bhattacharyya distance between the shape representations is used to find the point correspondences between the 2D fixed and moving images. The registration method involves parametric estimation of the non-linear diffeomorphism between the multimodal images and has its basis in solving a set of non-linear equations of thin-plate splines. The solution is obtained as the least-squares solution of an over-determined system of non-linear equations constructed by integrating a set of non-linear functions over the fixed and moving images. However, this may not result in clinically acceptable transformations of the anatomical targets. Therefore, the regularized bending energy of the thin-plate splines along with the localization error of established correspondences should be included in the system of equations. The registration accuracies of the proposed method are evaluated in 20 pairs of prostate mid-gland ultrasound and magnetic resonance images. The results obtained in terms of Dice similarity coefficient show an average of 0.980 ± 0.004, average 95% Hausdorff distance of 1.63 ± 0.48 mm and mean target registration and target localization errors of 1.60 ± 1.17 mm and 0.15 ± 0.12 mm respectively.

© 2012 Elsevier B.V. All rights reserved.

1. Introduction

Countries in Europe and USA have been following prostate cancer screening programs since the last 15 years (Andriole et al., 2009; de Koning et al., 2002; Roobol and Schroder, 2003). A patient with abnormal findings after a digital rectal examination, serum Prostate Specific Antigen (PSA) level over 4.0 ng/ml and PSA velocity more than 0.4–0.75 ng/ml/yr is generally advised for a prostate biopsy to diagnose the benign or malignant lesions from the histopathological examination of the prostate tissues. During needle biopsy, the most common appearance of malignant lesions in Transrectal Ultrasound (TRUS) is hypoechoic. The accuracy of sonographic finding of hypoechoic prostate cancer lesions is typically 43% (Carroll and Shinohara, 2010) and the prevalence of isoechoic prostate cancer lesions on TRUS ranges from 25% to 42%. The TRUS guided needle biopsy is performed using a multicore strategy where 10–12 samples are strategically extracted dividing the prostate into several regions (Porter et al., 2010). A hyper or hypoechoic lesion detectable with gray-scale TRUS is not necessarily a malignant lesion (Veltman et al., 2002). For instance, the chances of a hypoechoic lesion evaluated in TRUS guided biopsy being malignant is between 7% and 57% (Bogers et al., 1999). This results in multiple negative biopsies and thereby increases the number of re-biopsies required. In contrast, Magnetic Resonance Imaging (MRI) has a negative predictive value of 80–84% for significant cancer and the accuracy of MRI to diagnose prostate cancer is approximately 72–76% (Vilanova et al., 2011). Therefore, MRI may serve as a triage test for men deemed to be at risk of prostate cancer and may reduce the number of re-biopsies while at the same time provide more useful information for those who are sent for biopsy. Consequently, fusion of pre-biopsy MR images onto interoperative TRUS images might increase the overall biopsy accuracy (Hu et al., 2012; Kaplan et al., 2002; Singh et al., 2008; Xu et al., 2008). Fig. 1 shows the TRUS and the corresponding MR images of a prostate where the area within the circle marks a tumor that is isoechoic

---

* Corresponding author at: Computer Vision and Robotics Group, Universitat de Girona, Campus Montilivi, Edifici PIV, s/n, 17071 Girona, Spain. Tel.: +34 972 41 8876; fax: +34 972 41 8976.

E-mail addresses: jhimli.mitra@u-bourgogne.fr (J. Mitra), kato@inf.u-szeged.hu (Z. Kato), marly@eia.udg.edu (R. Martí), aoliver@eia.udg.edu (A. Oliver), llado@eia.udg.edu (X. Lladó), dro-desire.sidibe@u-bourgogne.fr (D. Sidibé), soumya.ghose@u-bourgogne.fr (S. Ghose), fabrice.meriaudeau@u-bourgogne.fr (F. Meriaudeau).
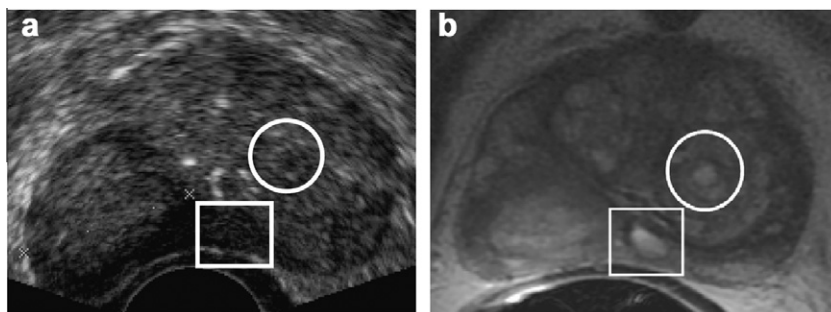
Fig. 1. TRUS and corresponding MR images of a prostate. (a) The area within the circle shows a tumor isoechoic with the normal prostate tissue inside the gland while that within the rectangle shows a hypoechoic tumor at the peripheral gland in the TRUS image, (b) the marked areas show the respective isoechoic and hypoechoic tumors with a different contrast than the normal prostate tissue in the MR image.

and the area within the rectangle is hypoechoic in TRUS, but can be seen with better contrast in the MR image.

The prostate of the same patient may undergo deformations under certain conditions. The inflation of the endorectal coil inside the rectum during MRI procedure, full bladder or bowel or gas inside the rectum, altered patient positions during the TRUS and MRI procedures may deform the prostate. In order to cope with these deformations, non-rigid registration methods (Alterovitz et al., 2004; Avants et al., 2008; Baumann et al., 2009; du Bois d'Aische et al., 2004; Chen et al., 2009; Mizowaki et al., 2002; Narayanan et al., 2009; Reynier et al., 2004; Xiao et al., 2010) need to be applied for prostate multimodal registration.

Spline-based deformations have been commonly used to register prostate images or volumes. The interpolating Thin-plate Splines (TPS) was originally proposed by Bookstein (1991) and involves the establishment of a set of point correspondences on a pair of images. However, these sets of correspondences are prone to error in real applications and therefore Rohr et al. (2001) extended the bending energy of TPS to approximation and regularization by introducing the correspondence localization error. Nevertheless, all these methods (Bookstein, 1991; Rohr et al., 2001) are dependant on a set of point correspondences on the pair of images to be registered. On the contrary, Domokos et al. (2012); Nemeth et al. (2009a,b) proposed a class of non-rigid registration that does not require explicit point correspondences and instead registers binary images solving a set of non-linear equations.

In this work, we have improved the generic non-linear registration framework of Domokos et al. (2012) by establishing prostate-specific point correspondences and regularizing the overall deformation. The point correspondences under the influence of which the thin-plate bends are established on the prostate contours by a method based on matching the shape-context (Belongie et al., 2002) representations of contour points using Bhattacharyya distance (Mitra et al., 2012). The approximation and regularization of the bending energy of the thin-plate splines are added to the set of non-linear TPS equations and are jointly minimized for a solution.

To evaluate the effects of the proposed extension to the existing framework of Domokos et al. (2012) we have compared our method against two variations; (1) the method of Domokos et al. (2012) where the TPS control points are placed on a uniform grid over the prostate mask images, and (2) the non-linear TPS deformation same as the previous, but with point correspondences established by our proposed method and without the approximation and regularization of bending energy. The proposed method is also evaluated against two commonly used spline-based deformable registration methods of TPS (Bookstein, 1991; Rohr et al., 2001) and B-splines (Rueckert et al., 1999).

The primary contributions of this paper may be summarized as follows:

1. The use of shape-context and Bhattacharyya distance (Mitra et al., 2012) to establish point correspondences on both fixed and moving images,
2. the use of a prostate-specific TPS transformation in the non-linear framework of Domokos et al. (2012),
3. and constraining the non-linear diffeomorphism by adding the approximation error and regularization of the TPS bending energy.

The remaining of the paper is organized as follows: Section 2 discusses some works related to the TRUS-MRI fusion and applications of spline-based registration methods for prostate images. Section 3 explains the proposed method of generating point correspondences and the system of non-linear diffeomorphic equations with the regularization, Section 4 provides the results of the experiments and comparisons with other methods. Section 5 presents a discussion related to the qualitative and quantitative registration results and accuracy of the proposed method followed by conclusions and further applications of the current method in Section 6.

2. Related work

Fusion of TRUS-MRI for guided needle biopsy of the prostate was reported by Kaplan et al. (2002) where a set of axial pre-biopsy MRI slices were rigidly registered with the axial ultrasound (US) images acquired during a transrectal biopsy procedure. The registration was driven by the minimization of the corresponding fiducials manually chosen in both the US and MR images. The experiment was validated with two patient datasets with only qualitative results provided as the results of the registration process.

An improved system was proposed by Reynier et al. (2004) for brachytherapy where manually segmented point clouds from MRI and TRUS were used to either rigidly or elastically align MRI with TRUS. The advantage of this system was the ability to model potential nonlinear deformation between the two modalities using octree splines (Szeliski and Lavallée, 1996). The elastic registration results were validated using 11 patient cases with an average residual distance of 1.11 ± 0.54 mm for surface points on TRUS and MRI.

Xu et al. (2008) presented a method for real-time registration of US and MRI for guided prostate biopsies. Before the biopsy procedure, a 3D TRUS volume (reconstructed from 2D axial sweep of the prostate with a US probe attached to a electro-magnetic tracker) was manually registered with a 3D MRI volume acquired previously using rigid body transformation. Thereafter an image based registration was employed for motion correction between the intra-operative 2D US frames and the reference US volume. A set of 2D frames within a short time frame were rigidly registered using

a sum-of-squared differences (SSD) based minimization with their respective 2D slices in the reference US volume. Finally, to further compensate for in-plane prostate motion the current 2D US frame and its corresponding reconstructed frame from the reference US volume was registered using an image gradient and correlation coefficient based registration. In patient studies for a new target the average time taken for biopsy was 101 ± 68 s. The registration method was validated on phantoms with a registration accuracy of 2.4 ± 1.2 mm. A total of 20 patient studies showed an average overlap between MRI and the US images as 90 ± 7% after motion compensation. The authors further validated their method with 101 patient cases (Kadoury et al., 2010) and the clinical results showed significant improvement of target visualization and of positive cancer detection rates during TRUS-guided biopsies.

Narayanan et al. (2009) proposed elastic registration between 3D TRUS and 3D MRI surfaces using adaptive focus deformable model (Shen et al., 2001) and elastic warping (Davatzikos, 1997) for localization of prostate biopsy targets. The average fiducial registration error was shown to be 3.06 ± 1.41 mm for 6 and 12 bead phantoms.

Hu et al. (2012) proposed a model-to-image registration method to fuse a patient-specific biomechanically simulated finite element-based statistical motion model of the pre-acquired MR volume with the TRUS volume during biopsy procedure. The deformable registration involved maximizing the likelihood of a particular model shape given a voxel intensity-based feature that provided an estimate of surface normal vectors at the boundary of the gland. The registration was constrained by the statistical motion model subspace. This statistical motion model subspace accommodated the random TRUS probe induced deformations of the gland. The median Root Mean Square (RMS) Target Registration Error (TRE) for 8 patients with 100 MR-TRUS registration experiments for each patient was found to be 2.40 mm.

Natarajan et al. (2011) also proposed elastic warping of MR volume to match the TRUS volume acquired for targeted prostate biopsy. The fusion method involves rigid alignment of the two volumes using manually selected anatomical landmarks and thereafter, the methods of Narayanan et al. (2009) and Karnik et al. (2010) were used for surface deformation. The MR-fusion based targeted biopsy was performed on 47 patients where a 33% biopsy-positivity rate was found versus a 7% positivity rate for systematic biopsy. The biopsy procedure took 15 min with an additional 5 min for the TRUS-MR fusion.

A recent work by Cool et al. (2011) suggested a pre-biopsy 3D TRUS-MR fusion with a landmark-based rigid registration and a subsequent deformable registration using TPS (Bookstein, 1991). Thereafter an image-based registration using the methods of Chrisochoides et al. (2006) and Ourselin et al. (2000) was performed to rigidly register the intra-biopsy 3D TRUS and pre-biopsy 3D TRUS (already co-registered with the pre-biopsy MR). The TRUS-TRUS rigid registration required 60 s. The MRI-TRUS fusion study was carried out on 19 patients with a retrospective study on five patients showing a mean TRE of 4.3 ± 1.2 mm. Prostate cancer was identified in 42% (8/19) of all patients having suspicious lesions.

TPS warping was also employed by Lu et al. (2000) to generate statistical volumetric model of the prostate for localization of prostate cancer. The registration error reported was too high to be considered for clinical procedures. The TRE for seven cases was reported to be 295.66 pixels, but the physical dimensions were not provided. Similarly, prostate MR volumes were warped using TPS by Fei et al. (2003) for brachytherapy and the registration was driven by the maximization of Normalized Mutual Information (NMI). The accuracy of the registration showed that the lowest prostate centroid displacement for a volume pair out of 17 volume pairs was 0.6 mm.

Cheung and Krishnan (2009) registered prostate MR volumes with and without the deformation of the endorectal coil using TPS with manually placed correspondences. Although the qualitative results were shown in terms of checkerboard overlap, the quantitative registration error was not reported. Daanen et al. (2006) used octree splines elastic registration to fuse TRUS and MRI prostate volumes for dosimetric planning of brachytherapy. The registration accuracy showed an average TRE of 2.07 ± 1.57 mm for four patients. Vishwanath et al. (2009) registered prostate histological slices and MR slices to detect prostate cancer using B-splines. Since the aim was to detect cancer, quantitative values related to registration accuracy were not presented. A recent work by Xiao et al. (2010) proposed to build a spatial disease atlas of the prostate using both B-splines and TPS. However, only qualitative results were presented.

Oguro et al. (2009) registered pre- and intra-operative MR images for prostate brachytherapy using B-splines based deformation. The Dice Similarity Coefficient (DSC) value for the total gland was reported as 0.91 and the fiducial registration error was 2.3 ± 1.8 mm for 16 cases. The accuracies of surface-based and image-based registration methods to register intra-session 3D TRUS-TRUS volumes were evaluated by Karnik et al. (2010). The surface-based registration involved a rigid registration using the iterative closest point algorithm (Besl and McKay, 1992) and the non-rigid registration was based on TPS. The image-based registration employed the block-matching technique of Ourselin et al. (2000) for rigid registration and the non-rigid deformation was defined by a 3D uniform grid of B-splines control points. A total of 16 patient datasets were used in the evaluation of the registration accuracies. The mean TRE for 60 fiducials for the TPS based registration was reported to be 2.09 ± 0.77 mm and for the B-splines based registration was found to be 1.50 ± 0.83 mm. TRUS and MR multimodal registration for TRUS interventional prostate biopsy was investigated by Mitra et al. (2012, 2010). The method in Mitra et al. (2010) was based on TPS with automatic point correspondences and provided an average DSC of 0.97 ± 0.01 for a limited cohort of 4 patient datasets. While, the method in Mitra et al. (2012) used B-splines registration driven by maximization of NMI of quadrature local energy of the multimodal images. The average DSC obtained was 0.943 ± 0.039 for 20 patients axial mid-gland slices, with an average TRE of 2.64 ± 1.37 mm obtained for 18 patients.

Analyzing the state-of-the art methods that exist for prostate TRUS-MR image registration or are based on spline-based transformations, we observe that many methods provided clinically significant registration accuracies, while some methods provided target registration accuracies greater than 3 mm. The methods that reported the gland overlap accuracies exhibited significantly poor overlap (approx. 90%). Additionally, few methods also required manual intervention at some stage to drive the registration procedure. In contrast, our proposed deformable registration method is automatic and capable of providing improved global and local registration accuracies that seem to be necessary for TRUS-guided biopsy procedure.

3. Method and materials

The aim of this work is to register a TRUS prostate image acquired during biopsy with a pre-acquired MR image of the same patient. Since the current proposition is to ascertain the feasibility and accuracy of the registration algorithm for biopsy procedures, the method requires an initial step of finding the MR slice corresponding to the axial TRUS slice under observation. This is not discussed here and may be accomplished by using an electromagnetic (EM) tracker attached to the TRUS biopsy probe (Xu et al., 2008) or

a 3D US-based tracking system (Baumann et al., 2012). Slice correspondences are therefore determined manually by an expert for the proposed research.

In this work, after the TRUS-MR slice correspondences are established, the prostate is manually segmented from the respective modalities. Although, our research team is investigating on automatic prostate segmentation methods from both TRUS and MRI (Ghose et al., 2011a, 2010, 2011b), we use manual segmentation to avoid incorporating the segmentation errors in the evaluation of the registration algorithm. The choice of an automatic or semi-automatic prostate segmentation method can be made from the review paper published by Zhu et al. (2006). The point correspondences required for the algorithm are established by the method explained in Section 3.1.1. The non-linear registration as described in Section 3.1.2 involves TPS transformation of the moving MR image non-linearized by a set of polynomial functions. The registration process aims to minimize the difference between the fixed image and the TPS transformed moving image both non-linearized by the same set of polynomial functions. In addition, the TPS bending energy is minimized with a regularization and considers the localization errors of the point correspondences. The sche-

ma of the proposed registration method is shown in Fig. 2. The rectangles in dotted lines represent the point correspondences method of Section 3.1.1 and the overdetermined system of equations for the non-linear registration framework of Section 3.1.2 respectively.

3.1. Method

3.1.1. Shape-contexts and point correspondences

The segmented prostate contour points are uniformly sampled using fixed Euclidean distance of ε i.e. if c_i is a contour point, $i = 1, \ldots, N$, then find the number of points N_s such that

$$\arg\max_j \lfloor c_i - c_j \rfloor^2 \leqslant \varepsilon, \quad i \neq j. \tag{1}$$

Fig. 3 shows the uniformly sampled segmented contours on the TRUS and MR images.

Let the number of uniformly sampled points now be represented as n, then each sample point c_i may be represented by a shape descriptor that is a $n - 1$ length vector of log-polar relative distances to points c_j, where $i \neq j$. The shape descriptor is binned

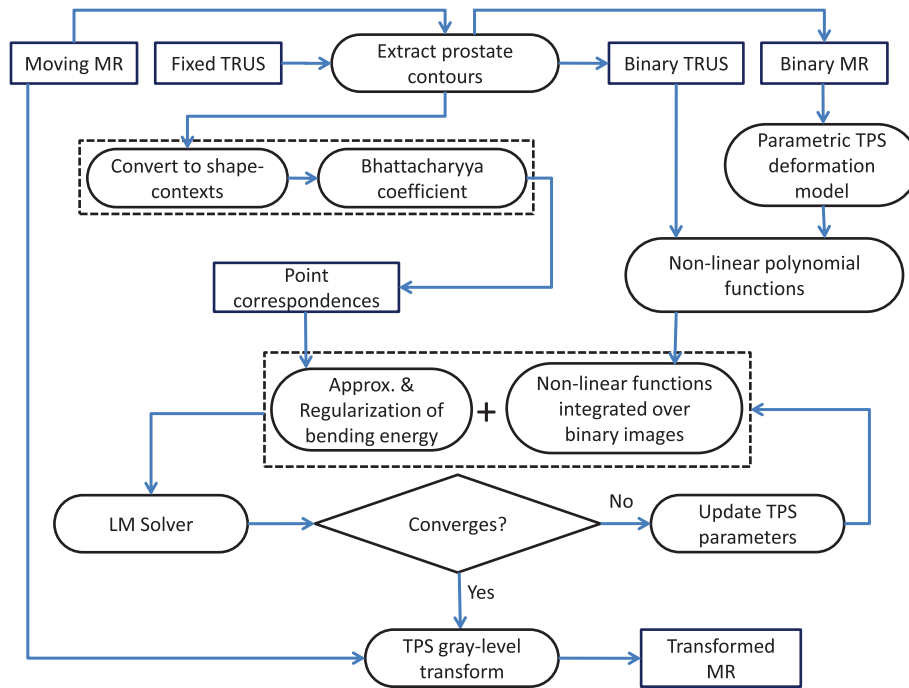

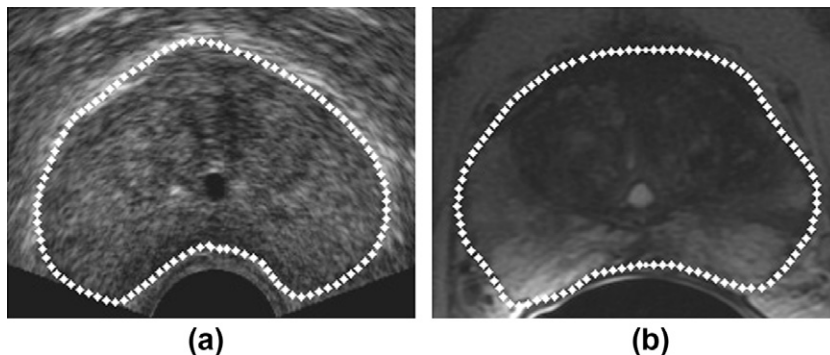**Fig. 2.** Schema diagram of the proposed registration framework.

Fig. 3. Uniformly sampled contours. (a) and (b) are the uniformly sampled segmented prostate contours on the TRUS and MR images respectively.

into a histogram that is uniform in log-polar space and this histogram is the shape-context representation of a contour point (Belongie et al., 2002) i.e. c_i is represented by a histogram $h_i(k, \theta)$ such that

$$h_i(k, \theta) = \#\{c_j, i \neq j : (c_i - c_j) \in bin(k, \theta)\}. \qquad (2)$$

k is the $\log r = \log(\sqrt{(x_{i1} - x_{j1})^2 + (x_{i2} - x_{j2})^2})$ and $\theta = \tan^{-1}\frac{x_{j2} - x_{i2}}{x_{j1} - x_{i1}}$ of the relative distance $(c_i - c_j)$, where, $c_i = (x_{i1}, x_{i2})$ and $c_j = (x_{j1}, x_{j2})$. As suggested by Belongie et al. (2002), a total of 5 bins are considered for k and 12 bins for θ that ensures that the histogram is uniform in log-polar space. This also means that more emphasis is given to the nearby sample points than those that are far away.

In the original work of Belongie et al. (2002), the point correspondence between two shapes is obtained by a bipartite graph matching method. However, in this work we choose to compute the Bhattacharyya distance (Bhattacharyya, 1943) between the shape-context histograms of two shapes to find the point correspondences. The bipartite graph matching using the Hungarian method (Papadimitriou and Stieglitz, 1982; Jonker and Volgenant, 1987) is robust with $O(n^3)$ time complexity in finding point correspondences in shapes which are significantly different and belong to different shape categories (Belongie et al., 2002) e.g. correspondences between bird and elephant or bone and apple, etc. However, we considered the Bhattacharyya distance since, it finds point correspondences with $O(n^2)$ time complexity and is sufficient for shapes such as prostate contours in TRUS and MRI which do not significantly differ from each other except for some deformation. Thus, to match a point c_i in a shape to a point c'_j in another shape, the Bhattacharyya coefficients between the shape-context histograms of c_i and all c'_j are computed and the c'_j that maximizes the relation in Eq. (3) is chosen as the corresponding point.

$$\arg\max_{c'_j} \sum_{k=1}^{5} \sum_{\theta=1}^{12} \sqrt{h_i^N(k, \theta).h_j'^N(k, \theta)}, \qquad (3)$$

where, $h_i^N(k, \theta)$ and $h_j'^N(k, \theta)$ are the normalized shape-context histograms of c_i and c'_j respectively.

Fig. 4 shows the log-polar bins of a histogram, the histograms of a point correspondence in two shapes and the contour correspondences overlaid on the TRUS and MR prostate shapes. Fig. 5 additionally shows some examples where the prostates are significantly deformed in the MR image than the TRUS image. Nonetheless, Bhattacharyya distance could successfully extract point correspondences on the prostate contours.

The first point correspondence established on both the TRUS and MR prostate boundaries is marked with a '☆' in the posterior part of the axial gland in Fig. 4b and c respectively. This point is obtained in the TRUS image as the intersection point of the longitudinal principal axis with the boundary. The first two principal axes are computed from the principal component analysis of all the contour points of the prostate shape in TRUS. The 8 point correspondences are chosen on the prostate boundary with the rationale of capturing the inflexions of the prostate curve. Therefore, once the first point at the posterior part of the gland is defined on the TRUS boundary, the remaining seven points are automatically placed dividing the total number of uniformly sampled contour points by 8. Thereafter, the 8 point correspondences are searched for in the MR image using the afore-mentioned method.

It is evident from the Fig. 4b and c respectively that the correspondences are explicitly defined on the prostate contours. Therefore, the regularization of the correspondences will not take the correspondences inside the prostate gland into account and may cause deformations of the gland that are not acceptable for clinical procedures. Hence, the prostate centroids and 4 other points that are the midpoints of the straight lines between '☆' and '+', '+' and '×', '×' and '◇' and '◇' and '☆' respectively are considered (see Fig. 6). The manner in which the internal points are formed i.e. by the mid-points of the lines joining the boundary control points in alternating sequence starting from the first point ('☆'), is necessary to ensure that the control points are placed inside
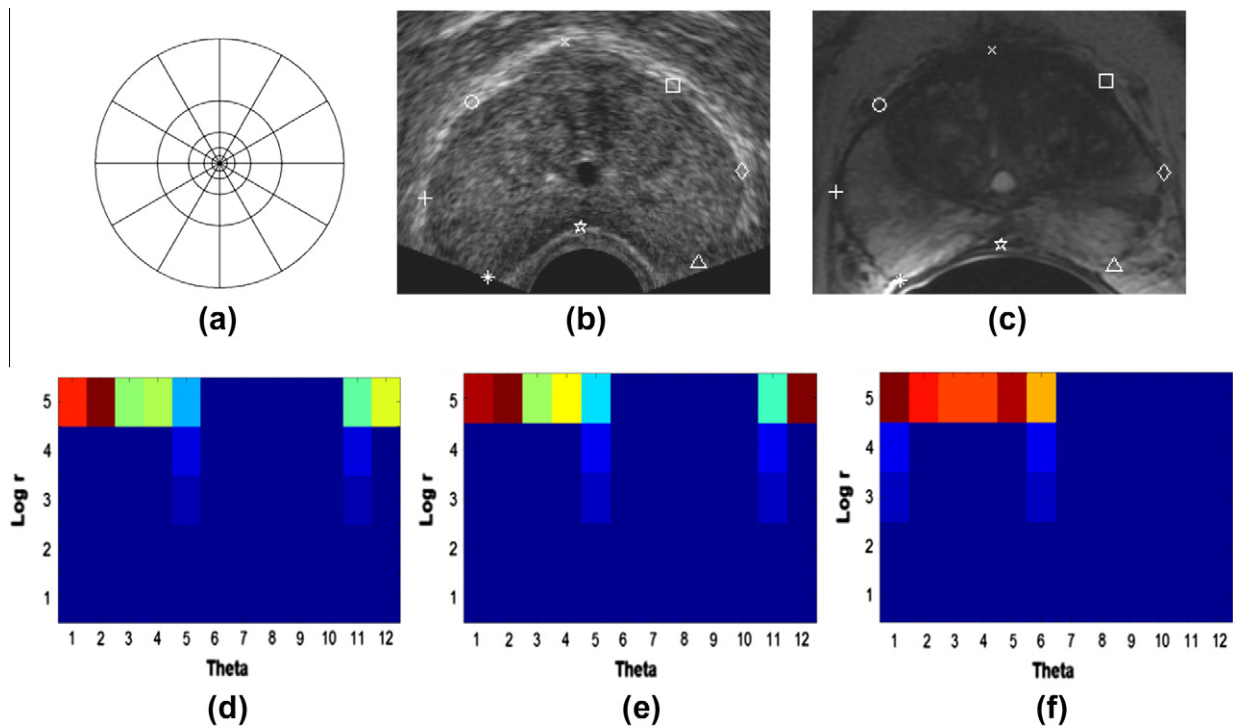
Fig. 4. Point correspondences example. (a) Log-polar histogram bins; (b) contour points in TRUS; (c) point correspondences of (b) in MR; (d) log-polar shape-context histogram of '○' in (b); (e) log-polar shape-context histogram of '○' in (c); both (d) and (e) show visual correspondence; (f) histogram of '×' in (c) does not show visual correspondence with histogram in (d). The x–y axes in the log-polar shape-context histograms correspond to θ and $\log r$ respectively.
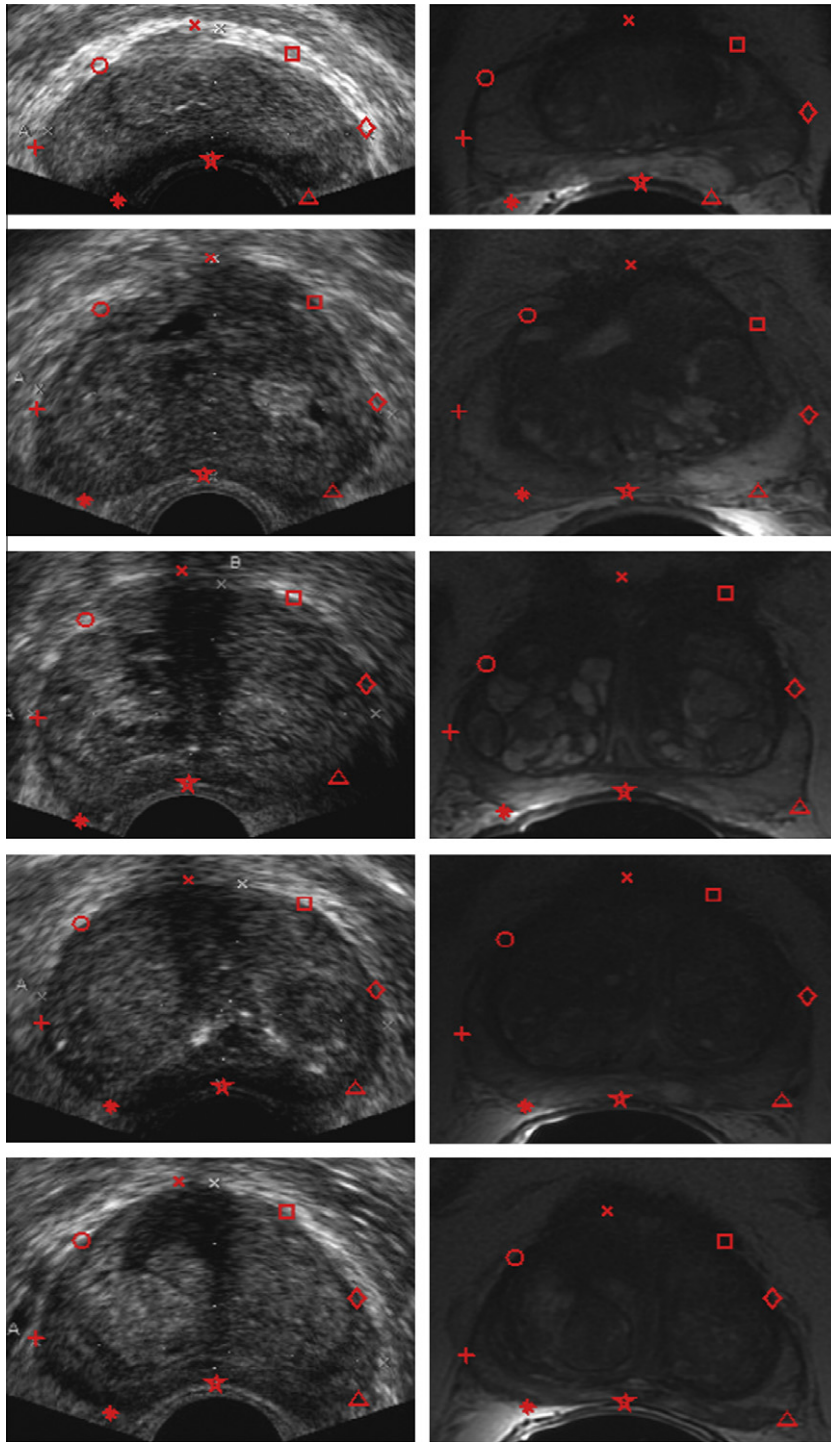
Fig. 5. Point correspondences on TRUS and MR prostate contours using Bhattacharyya distance. The left column shows the TRUS images and the right column shows the MR images. The MR images show deformed prostates than those on the TRUS images. The 8 point correspondences are marked in 'red'. (For interpretation of the references to colour in this figure legend, the reader is referred to the web version of this article.)

the prostate gland and yet not too close to the boundary control points. The 13 point correspondences finally established may be termed as p_i, where, $i = 1, \ldots, 13$ for further references.

3.1.2. Non-linear diffeomorphism

To align a pair of binary shapes, let us consider the moving and the fixed images be $\mathbf{x} = [x_1, x_2] \in \mathbb{R}^2$ and $\mathbf{y} = [y_1, y_2] \in \mathbb{R}^2$ respectively, such that there exists a bijective transformation $\varphi(.)$ between the images as

$$\mathbf{y} = \varphi(\mathbf{x}) \iff \mathbf{x} = \varphi^{-1}(\mathbf{y}). \tag{4}$$

The deformation field $\varphi(.)$ can be decomposed for the 2D coordinates respectively as $\varphi(\mathbf{x}) = [\varphi_1(\mathbf{x}), \varphi_2(\mathbf{x})]$, where $\varphi_1, \varphi_2 : \mathbb{R}^2 \to \mathbb{R}$. If explicit point correspondences are not established then the diffeomorphism is obtained by integrating over the foreground pixels of the fixed and moving image domains I_f and I_m respectively (Domokos et al., 2012):
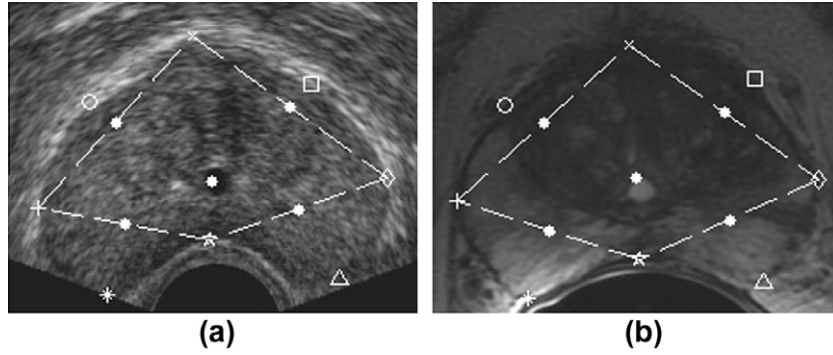
Fig. 6. Point-set of correspondences on TRUS and MR images. Correspondences inside the prostate are shown by white '•'s. The dashed line signifies that the white '•' falling on the line is the mid-point of the same joining the correspondences established on the contour.

$$\int_{I_f} \mathbf{y}\,d\mathbf{y} = \int_{I_m} \varphi(\mathbf{x})|J_\varphi(\mathbf{x})|d\mathbf{x}, \tag{5}$$

where the integral transformation $\mathbf{y} = \varphi(\mathbf{x})$ and $d\mathbf{y} = |J_\varphi(\mathbf{x})|d\mathbf{x}$. $|J_\varphi| : \mathbb{R}^2 \to \mathbb{R}$ is the Jacobian determinant of the transformation at each foreground pixel of the moving image as

$$|J_\varphi(\mathbf{x})| = \begin{vmatrix} \frac{\partial \varphi_1}{\partial x_1} & \frac{\partial \varphi_1}{\partial x_2} \\ \frac{\partial \varphi_2}{\partial x_1} & \frac{\partial \varphi_2}{\partial x_2} \end{vmatrix} \tag{6}$$

It is to be noted that the identity relation of Eq. (4) is also valid under the influence of a set of non-linear functions $\omega_k(.) : \mathbb{R}^2 \to \mathbb{R}$, $k = 1, \ldots, l$ (Domokos et al., 2012), acting on both sides of Eq. (5) as

$$\int_{I_f} \omega_k(\mathbf{y})d\mathbf{y} = \int_{I_m} \omega_k(\varphi(\mathbf{x}))|J_\varphi(\mathbf{x})|d\mathbf{x}. \tag{7}$$

Therefore to estimate the parameters of the transformation the number of non-linear functions l, must be larger than the number of parameters to generate a set of linearly independent equations.

In this work, the underlying transformation is considered to be the radial-basis function of TPS where the foreground pixels of the moving image deform under the influence of the control points $p_i \in \mathbb{R}^2$ established by the method of Section 3.1.1. The TPS transformation may be written as

$$\varphi_v(\mathbf{x}) = a_{v1}x_1 + a_{v2}x_2 + a_{v3} + \sum_{i=1}^{n} w_{iv}U(p_i - \mathbf{x}), \tag{8}$$

where, $i = 1, \ldots n$, $v = 1, 2$, $U : \mathbb{R} \to \mathbb{R}$ is the radial-basis function as $U(r) = r^2 \log r^2$, a_{v1}, a_{v2} and a_{v3} are the 6 affine parameters and w_{iv} are the $2n$ TPS weight parameters for the control points. The additional constraints for the TPS interpolation are that the sum of the weights applied to the plate as well as moments with respect to both axes should be 0 to ensure that the plate will not deform under the action of the loads and are given as

$$\sum_{i=1}^{n} w_{iv} = 0 \text{ and } \sum_{i=1}^{n} p_{iu}w_{iv} = 0, u, v = 1, 2. \tag{9}$$

If, $\varphi : \mathbb{R}^2 \to \mathbb{R}^2$, $\varphi(\mathbf{x}) = [\varphi_1(\mathbf{x}), \varphi_2(\mathbf{x})]^T$ represents a TPS map with $6 + 2n$ parameters, then the Jacobian $J_\varphi(\mathbf{x})$ is composed of the partial derivatives (Domokos et al., 2012) given below ($u, v = 1, 2$)

$$\frac{\partial \varphi_v}{\partial x_u} = a_{vu} - \sum_{i=1}^{n} 2w_{iv}(p_{iu} - x_u)\left(1 + \log(\|p_i - \mathbf{x}\|^2)\right) \tag{10}$$

where, $\|.\|$ is the Euclidean norm.

However, the transformation of Eq. (8) when replaced in Eq. (7) will only consider the point set on the moving image under the influence of which the image deforms to match the fixed image, therefore, the gray-level deformations of the regions inside the

prostate may not be meaningful for clinical applications. The correspondences p_i, established across the fixed and moving image domains as $p_i^f = \left[p_{y_{i1}}^f, p_{y_{i2}}^f\right]$ and $p_i^m = \left[p_{x_{i1}}^m, p_{x_{i2}}^m\right]$, $i = 1, \ldots, n$ respectively, play an important role in constraining these deformations. We introduce the bending energy of the TPS along with the correspondence localization errors (Rohr et al., 2001) as an additional constraint to solve the set of equations in Eq. (7) as

$$E_{TPS} = \int_i \int_i \left[\left(\frac{\partial^2 \zeta}{\partial p_{x_{i1}}^m{}^2}\right)^2 + 2\left(\frac{\partial^2 \zeta}{\partial p_{x_{i1}}^m \partial p_{x_{i2}}^m}\right)^2 + \left(\frac{\partial^2 \zeta}{\partial p_{x_{i2}}^m{}^2}\right)^2 \right] \partial p_{x_{i1}}^m \partial p_{x_{i2}}^m, \tag{11}$$

where, $\zeta : \mathbb{R}^2 \to \mathbb{R}^2$, $\zeta = \left[\zeta_1(p_i^m), \zeta_2(p_i^m)\right]$ is the transformation of the point correspondences established on the moving image to match with those of the fixed image.

$$\zeta = \zeta_v(p_i^m) = a_{v1}p_{x_{i1}}^m + a_{v2}p_{x_{i2}}^m + a_{v3} + \sum_{j=1}^{n} w_{jv}U(p_i^m - p_j^m), v = 1, 2. \tag{12}$$

The 1st and 3rd terms in Eq. (11) may be written analytically as follows:

$$\frac{\partial^2 \zeta_v}{\partial p_{x_{iu}}^m{}^2} = \sum_{j=1}^{n} 2w_{jv} \left[1 + \log(\|p_i^m - p_j^m\|^2) + \frac{2(p_{x_{iu}}^m - p_{x_{ju}}^m)}{\|p_i^m - p_j^m\|^2} \right], \quad u = 1, 2 \tag{13}$$

and the 2nd term in Eq. (11) can be written as

$$\frac{\partial^2 \zeta_v}{\partial p_{x_{i1}}^m \partial p_{x_{i2}}^m} = \sum_{j=1}^{n} 4w_{jv} \left[\frac{(p_{x_{i1}}^m - p_{x_{j1}}^m)(p_{x_{i2}}^m - p_{x_{j2}}^m)}{\|p_i^m - p_j^m\|^2} \right], \quad v = 1, 2. \tag{14}$$

Finally, the equation acting as a constraint is the regularized TPS bending energy with the quadratic approximation term that considers the correspondence localization error is

$$\frac{1}{n} \sum_{i=1}^{n} \frac{\left\| p_i^f - \zeta(p_i^m) \right\|^2}{\sigma_i^2} + \lambda E_{TPS} = 0, \tag{15}$$

where, σ_i^2s are sum of the variances of the correspondences between the fixed and moving images i.e. $\sigma_i^2 = \sigma_i^{f^2} + \sigma_i^{m2}$. The parameter λ is a regularization factor set with a small value 0.0001 that ensures that the thin-plate adapts well to the deformation of the local structures (Rohr et al., 2001). Finally, $\zeta(p_i^m)$ is obtained from Eq. (12) and E_{TPS} from Eq. (11).

The adopted set of non-linear functions in Eq. (7) are the power functions as proposed in Domokos et al. (2012)

$$\omega_k(\mathbf{x}) = x_1^{a_k} x_2^{b_k}, \tag{16}$$

with $(a_k, b_k) \in \langle (0,0), (1,0), (0,1), (1,1), (2,0), (0,2), (2,1), (1,2), (2,2), \ldots, (6,6) \rangle$. The total number of parameters to be estimated is 32 that comprises of 6 affine and 13×2 TPS weight parameters for 13 correspondences. Therefore, 49 linearly independent equations are generated using the power set of $\omega_k(.)$ functions with additional 4 equations for Eq. (9) and one for Eq. (15). The solution to the set of non-linear equations i.e. Eq. (7), Eq. (9) and Eq. (15) is obtained using *Levenberg–Marquardt* (LM) algorithm (Marquardt, 1963). It is to be noted that depending on the ω_k functions in Eq. (7), numerical instability may arise due to the summation of the polynomial functions, i.e. the power functions $\omega_k(.)$ act on the set of coordinate values of the images, therefore summing up the coordinate values (raised by some factor) would result in very large values. In order to solve this problem, the foreground pixels of the moving and fixed images are normalized within a unit square $[-0.5, 0.5] \times [-0.5, 0.5]$ so that the shape centers become the origins while the range of ω_k functions are chosen within the interval $[-1, 1]$. A detailed explanation on the normalization of the image coordinates and the interval of $\omega_k(.)$ functions is provided by Domokos et al. (2012).

3.2. Materials

The TRUS images were acquired using a 6.5 MHz side-firing probe with SIEMENS Allegra and TOSHIBA Xario machines and the axial T2 fast relaxation fast spin echo MRI slices with slice thickness of 3 mm, repetition time of 3460–3860 ms and echo time of 113.62–115.99 ms were acquired with a 1.5 Tesla GE Signa HDxt. Prostate mid-gland images of 20 patients with average prostate volume of 56.7 ± 22.0 cm^3 are used for the evaluation of our algorithm. The prostate images used for the experiment have an average size of 249×219 pixels with a pixel dimension being 0.2734 mm $\times$ 0.2734 mm. The axial middle slices in TRUS are chosen for which the corresponding axial MR slices are identified by one expert radiologist and one expert urologist. The axial TRUS slice may not always have the exact orientation of the MR axial slices since the TRUS probe orientation is unknown. Therefore, instead of quantifying the probe angle in our experiment, we validated the algorithm on those axial TRUS slices that seem to be parallel with the axial MR slices as identified by the experts. Axial sweeps of the prostate gland from base to apex/mid-gland are only available for 2 patient cases in TRUS whose corresponding MR slices could also be identified. Therefore, these two cases are used to show the accuracy of the proposed registration method for off-mid-gland TRUS-MR slices. The prostates are manually segmented from both the moving MR and fixed TRUS images. The image backgrounds are removed and only a region of interest i.e. the prostate is used for the evaluation of the algorithm. The proposed point correspondence and registration methods were implemented on MATLAB 2009(b) and were run on an Intel Core2Duo 1.66 GHz processor with 2 GB RAM.

4. Experiments and results

The TRUS slice is the fixed image and the respective MR slice is the moving image for all the experiments. The registration accuracies that measure overlap are evaluated in terms of Dice Similarity Coefficient (DSC) (Dice, 1945) and 95% Hausdorff Distance (HD) (Huttenlocher et al., 1993). Local registration accuracies of anatomical structures inside the prostate gland are measured by Target Registration Error (TRE) and Target Localization Error (TLE) (Maurer et al., 1993; Maurer et al., 1997).

DSC is a measure of overlap of the same foreground labels (E) between the transformed moving image ($M(E)$) and the fixed image ($F(E)$) and is given by

$$\text{DSC} = \frac{2(M(E) \cap F(E))}{M(E) + F(E)}. \tag{17}$$

This means that a high DSC ($> 90\%$) signifies a good overlap between the prostate regions after registration.

Given a finite set of points $A = \{a_1, \ldots, a_p\}$ and $B = \{b_1, \ldots, b_q\}$, the Hausdorff distance between the point sets is defined by

$$HD(A, B) = \max(h(A, B), h(B, A)) \tag{18}$$

where

$$h(A, B) = \max_{a \in A}(\min_{b \in B}\|a - b\|) \tag{19}$$

The HD measure plays a significant role in identifying the similarity between the deformed moving image contour and the fixed image contour. A low value of HD signifies good contour registration accuracy. Therefore, even if a DSC measure signifies good region overlap, the HD measure may not signify a good contour registration.

A target is an anatomical landmark in the patient's body and is normally the centroid of a lesion, tumor, gland, etc. that is not used to compute the transformation of the moving image to the fixed image. TRE is the root mean square distance of such homologous targets tp_i and $tq_i, i = 1, 2, \cdots, N$ on the moving and the fixed images respectively and is given by

$$\text{TRE} = \frac{1}{N}\sqrt{\sum_{i=1}^{N}(\mathbf{T}(tp_i) - tq_i)^2} \tag{20}$$

where, $\mathbf{T}(.)$ is the transformation of the moving image. The targets used in our experiments are primarily the centroids of lesions and tumors in the central gland, the prostatic urethra, sometimes the centroids of tumors in the peripheral region and the centroid of the central gland in few cases where lesions or other homologous structures are not visible in TRUS as in the corresponding MRI. One target for each pair of TRUS and MR image is used for the experiments. The repeatability error in the localization of the targets is given as the TLE computed from the centroids of manually selected regions from five independent trials by an experienced radiologist and an experienced urologist. A low TRE and a low TLE values signify good local registration accuracy. The clinical significance of TRE is the accuracy in identifying the anatomical targets in the deformed moving image. Actual TRE values may also incorporate TLE values, which is useful for clinical purposes to avoid underestimation of the true TRE values.

Various experiments are performed owing to the selection criteria of the number of boundary and internal control points for a smooth and accurate deformation of the prostate gland and its internal structures. The validations of such experiments with varying number of control points are shown in Section 4.1. The experimental results with different registration methods are shown in Section 4.2. The validation of registration accuracies on a subset of patients when automatic segmentation is used is shown in Section 4.3 and experimental results for the validation of the proposed registration method for off mid-gland slices are shown in Section 4.4. A comprehensive statistical analysis of the results is presented in Section 4.5.

4.1. Control points

As mentioned in Section 3.1.1 that a total of 8 point correspondences are required on the boundary and 4 internal points along with 1 point on the prostate centroid for a smooth deformation. Therefore, to validate the number of boundary and internal points, several experiments are performed with less and more than 8 boundary points along with the internal points generated in an alternating manner as mentioned in Section 3.1.1.

The first experiment is done with only 6 points on the boundary and the internal points are generated accordingly as the mid-points of the lines joining the alternate boundary points starting from the first point '☆' as shown in Fig. 7. It can be seen clearly from Fig. 7a and b respectively that the inflexion points at the posterior parts of the prostate axial slices are not captured properly.

The following experiment is done increasing the number of boundary points from 8 (proposed) to 10. Accordingly the internal points are also generated. Fig. 8a and b show the 10 boundary and five internal points along with one prostate centroid. Although the boundary has several points to capture the inflexions of the prostate curve, the internal points generated are placed near the boundaries. This may result in distorted deformations of the prostate internal structures.

Finally an experiment is performed using eight boundary points without any internal points or centroid. Fig. 9a and b show the point correspondences placed on the boundary for the TRUS and the MR prostate images respectively. Table 1 shows the registration accuracies in terms of DSC, TRE and TLE for the experiments performed with varied number of control points for all 20 patient cases. M1 is defined for six boundary points and four internal points, M2 is defined for 10 boundary points and 6 internal points and M3 is defined for eight boundary points and no internal points. These abbreviations are being consistently used in the remaining document. As shown by the DSC values of Table 1 that with varying point correspondences on the boundary, the global registration accuracies do not change significantly by the virtue of the diffeomorphic function. However, the local registration accuracies measured in terms of TRE have a lot of variation between the different methods M1, M2 and M3 respectively. Fig. 10 shows the qualitative registration results using the proposed method with different sets of control points for patient 6. Although the qualitative results with

M1 and M2 (rows 2 and 3) do not show significant differences with the proposed eight boundary and five internal points (last row), the unconstrained deformation in the absence of the internal points is seen for the method M3 (row 4), i.e. the prostatic urethra in the deformed image is away from that on the fixed image.

4.2. Registration methods

The proposed method and its two variants as mentioned in Section 1 are replaced by acronyms for further references as NLTPS-REGCORR (proposed), NLTPS-UNI (non-linear TPS with control points placed on a uniform grid) and NLTPS-CORR (non-linear TPS with proposed point correspondences without regularization of bending energy) respectively. The method in NLTPS-REGCORR and NLTPS-CORR use 13 point correspondences established by the method in Section 3.1.1. A total of 16 uniform grid-points are used for NLTPS-UNI. We have quantitatively compared the registration results of NLTPS-REGCORR against NLTPS-UNI, NLTPS-CORR, traditional TPS (Rohr et al., 2001) and B-splines (Rueckert et al., 1999) method with their global registration accuracies in terms of DSC, 95% HD, local registration accuracies in terms of TRE, TLE and timing requirements in Tables 2 and 3 respectively. The traditional TPS (Rohr et al., 2001) registration method is used with a total of 32 point correspondences on the boundary with five internal points as discussed in Mitra et al. (2010). The B-splines registration follows a multiresolution framework in three spatial resolutions and uses uniform control grids with 16×16 pixel spacing in the final resolution (Kroon, 2008). Table 3 also shows the number of uniform control grids used for the B-splines (Rueckert et al., 1999) registration. It is to be noted that the traditional TPS requires a total of 37 point correspondences to provide a smooth transformation, while our proposed method can perform well with

Fig. 7. 6 point correspondences on the boundary with 3 internal points and 1 point on prostate centroid. The '☆'s mark the first set of point correspondences on the boundary. (a) Point sets on the TRUS image, (b) corresponding points of TRUS image on the MR prostate image.
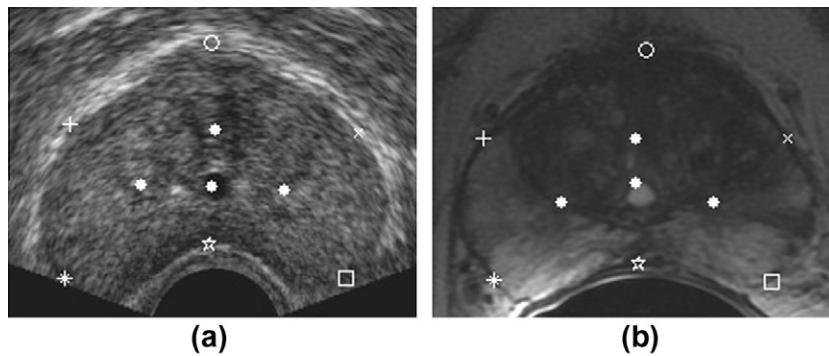

Fig. 8. 10 point correspondences on the boundary with five internal points and one point on prostate centroid. The '☆'s mark the first set of point correspondences on the boundary. (a) Point sets on the TRUS image, (b) corresponding points of TRUS image on the MR prostate image.

Fig. 9. 8 point correspondences on the boundary with no internal points or centroid. The '☆'s mark the first set of point correspondences on the boundary. (a) Point sets on the TRUS image, (b) corresponding points of TRUS image on the MR prostate image.
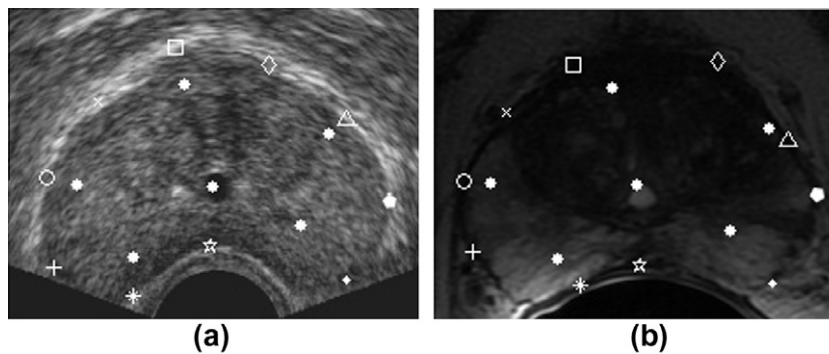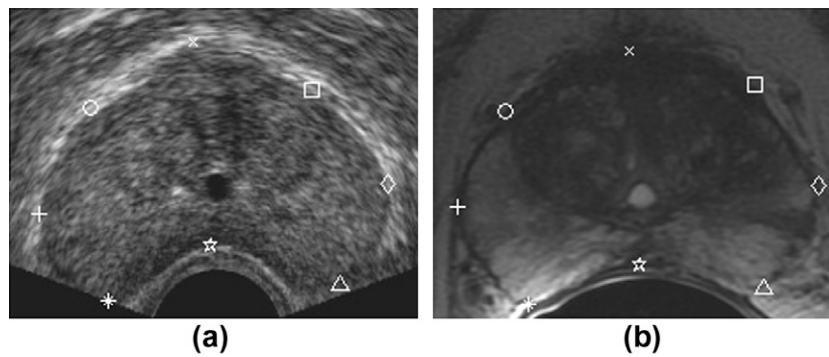
Table 1
A comparison of global and local registration accuracies for the proposed method with varying control points. M1 is the acronym for 6 boundary points and 4 internal points, M2 is the acronym used for 10 boundary points and 6 internal points and M3 is the acronym used for 8 boundary points and no internal points. P# represents the patient number, μ is the mean and σ is the standard deviation of the measures. A high DSC value signifies good global registration accuracy, while a low TRE and TLE signifies good local registration accuracies around anatomical landmarks.

| P#	Varying point correspondences								
	M1			M2			M3		
	DSC	TRE (mm)	TLE (mm)	DSC	TRE (mm)	TLE (mm)	DSC	TRE (mm)	TLE (mm)
1	0.974	1.08	0.23	0.957	2.79	0.09	0.968	2.37	0.25
2	0.985	1.78	0.06	0.985	1.46	0.05	0.978	1.29	0.05
3	0.980	2.29	0.07	0.981	1.22	0.04	0.980	0.98	1.14
4	0.986	3.01	0.50	0.988	2.39	0.30	0.984	1.85	0.84
5	0.984	0.79	0.05	0.979	0.59	0.07	0.978	1.39	0.95
6	0.970	0.39	0.03	0.973	0.26	0.04	0.971	1.76	0.05
7	0.984	3.89	0.09	0.982	3.60	0.12	0.985	12.05	0.03
8	0.981	5.59	0.20	0.984	2.08	0.58	0.981	2.30	0.32
9	0.983	1.33	0.28	0.981	1.98	0.15	0.981	1.87	0.24
10	0.985	3.98	0.05	0.986	4.03	0.04	0.986	4.15	0.03
11	0.983	2.38	0.08	0.982	1.93	0.08	0.980	2.81	0.05
12	0.982	1.15	0.26	0.982	0.98	0.32	0.981	1.33	0.26
13	0.984	3.84	0.06	0.981	5.21	0.05	0.983	5.64	0.07
14	0.982	0.65	0.04	0.986	0.46	0.02	0.986	2.52	0.04
15	0.984	14.05	0.08	0.982	14.07	1.10	0.984	17.40	0.07
16	0.985	2.91	0.09	0.979	1.44	0.08	0.980	2.08	0.10
17	0.981	2.12	0.28	0.982	1.87	0.19	0.984	2.45	0.16
18	0.977	0.67	0.30	0.980	1.42	0.28	0.980	0.60	0.33
19	0.979	1.96	0.08	0.979	2.05	0.04	0.978	1.36	0.17
20	0.976	0.76	0.21	0.982	1.13	0.36	0.984	0.60	0.19
μ	**0.981**	**2.73**	**0.15**	**0.981**	**2.55**	**0.20**	**0.981**	**3.34**	**0.27**
σ	**0.004**	**3.01**	**0.12**	**0.006**	**2.98**	**0.26**	**0.005**	**4.16**	**0.33**

The bold values signify the average and standard deviations for the registration accuracy and are of importance while evaluating the overall efficacy of the proposed method.

only 13 point correspondences. The traditional TPS finds the transformation as a solution to a least-squares problem. Any least-squares solution requires an over-determined system of equations to provide numerically stable solutions. Therefore, the traditional TPS uses more number of control points than our proposed method since only one equation is associated with each control point. On the contrary, a set of power function polynomials are involved with each control point for our method; thereby providing an over-determined system of equations with less number of control points. Since the B-splines of Rueckert et al. (1999) uses uniform control grid; therefore a consistent number of control points similar to the traditional TPS or the proposed method could not be used. Fig. 11 shows some results of the transformation using the methods NLTPS-UNI, NLTPS-CORR and NLTPS-REGCORR respectively. The results for patients 7, 8, 11 and 12 are shown in each column. Fig. 12 shows some of the results of TRUS-MR fusion with traditional TPS and B-splines and the corresponding results using our proposed method. The TPS uses point correspondences as described in Mitra et al. (2010) and the B-splines used uniform grids. The results for patients 1, 5, 15 and 17 are shown in columns. The

choice of a different set of patient cases for Fig. 12 ensures that more qualitative results obtained from the proposed algorithm are shown. Moreover, the results that are unbiased towards the proposed method and have acceptable registration accuracies when traditional spline-based methods are used are also presented.

4.3. Automatic segmentation

The registration methods as discussed in Section 4.2 are performed using manually segmented prostate contours for both the TRUS and MR images in order to avoid the automatic segmentation errors in the process of evaluating the registration accuracies. However, we have used 10 patient cases i.e. patients 5–14 among the 20 patients to evaluate the sensitivity of the registration accuracies when an automatic segmentation method is employed. The method of Ghose et al. (2011a) is used to segment the prostate from both the TRUS and MR images. Fig. 13 shows the final segmented contours in red lines for the TRUS and the MR images, the point correspondences placed accordingly and the qualitative
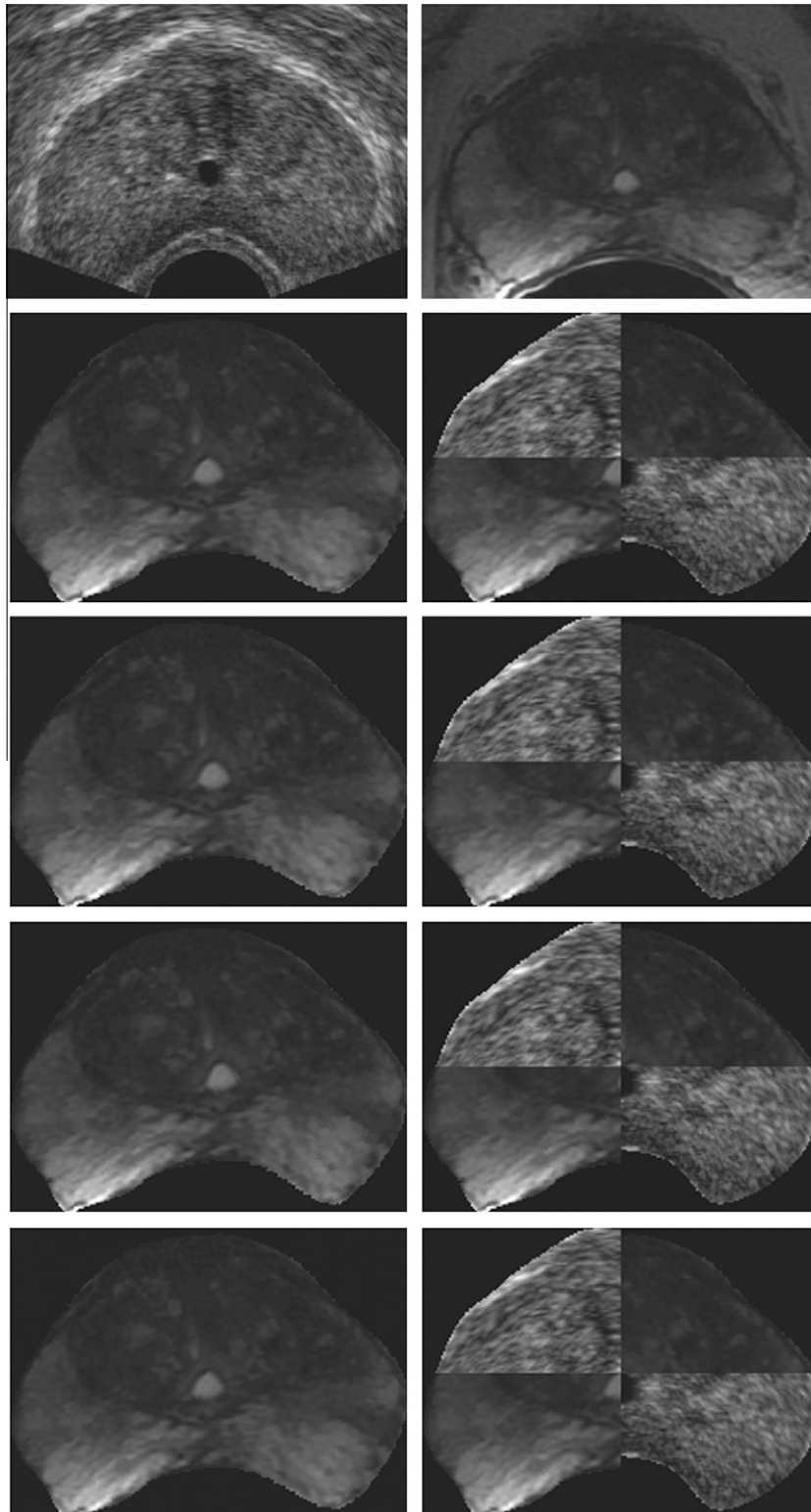
Fig. 10. Deformation of the prostate gland with different sets of control points for Patient 6. Row 1 shows the TRUS and the MR images, row 2, 3 and 4 show the qualitative results of methods M1, M2 and M3 respectively and row 5 shows the results with the proposed optimum set of control points.

registration results for the same patient case. It is observed from the figure that the automatic segmentation of the prostate contour in the MR image has the maximum overlap with the manual segmentation while a satisfactory overlap is obtained for the prostate contour in the TRUS image.

Table 4 shows the DSC, HD, TRE and TLE values for the 10 patients (patient 5–14). It is to be noted that despite some segmentation inaccuracies induced by the automatic segmentation process; the registration accuracies do not change significantly when compared to the registration with manually segmented contours.

Table 2
A comparison of registration accuracies of the non-linear TPS registration NLTPS-UNI, NLTPS-CORR, NLTPS-REGCORR, traditional TPS and B-splines respectively. μ is the mean and σ is the standard deviation of the measures. A high DSC and low TRE and TLE values signify good registration accuracy.

P#	NLTPS-UNI			NLTPS-CORR			NLTPS-REGCORR			TPS		Rohr et al. (2001)	B-splines		Rueckert et al. (1999)
	DSC	TRE (mm)	TLE (mm)	DSC	TRE (mm)	TLE (mm)	DSC	TRE (mm)	TLE (mm)	DSC	TRE (mm)	TLE (mm)	DSC	TRE (mm)	TLE (mm)
1	0.979	2.30	0.12	0.944	–	–	0.968	1.28	0.28	0.971	9.36	0.22	0.902	5.07	0.10
2	0.987	2.59	0.09	0.989	5.00	0.21	0.981	1.34	0.07	0.957	3.98	0.10	0.980	0.37	0.09
3	0.987	2.63	0.03	0.984	5.80	0.09	0.980	1.12	0.09	0.974	7.92	0.13	0.973	9.93	0.11
4	0.989	1.42	0.07	0.989	2.76	0.02	0.982	0.93	0.54	0.982	5.21	0.49	0.985	1.91	0.28
5	0.990	1.63	0.03	0.989	3.97	0.06	0.979	0.50	0.08	0.972	2.11	0.07	0.889	9.08	0.04
6	0.989	7.03	0.78	0.990	3.24	0.04	0.971	0.29	0.03	0.979	1.17	0.05	0.869	6.11	0.04
7	0.989	14.29	0.26	0.987	13.99	0.50	0.984	3.86	0.10	0.977	4.43	0.12	0.959	0.90	0.12
8	0.992	–	–	0.988	7.55	0.08	0.979	1.23	0.11	0.978	3.57	0.05	0.976	4.70	0.03
9	0.987	1.89	0.02	0.988	1.99	0.03	0.981	1.10	0.24	0.978	2.70	0.46	0.960	1.56	0.41
10	0.989	2.15	0.02	0.989	3.07	0.02	0.984	3.58	0.03	0.972	6.09	0.04	0.952	8.29	0.09
11	0.990	12.95	0.38	0.989	12.68	0.34	0.980	2.63	0.07	0.972	2.98	0.12	0.962	6.12	0.04
12	0.982	1.11	0.05	0.980	1.35	0.12	0.981	0.94	0.21	0.971	2.44	0.12	0.944	1.58	0.25
13	0.985	7.47	0.33	0.986	6.22	0.34	0.983	4.54	0.07	0.980	3.06	0.07	0.961	1.00	0.05
14	0.989	10.64	0.28	0.991	7.28	0.21	0.986	0.24	0.05	0.986	1.75	0.07	0.896	7.32	0.05
15	0.987	1.60	0.09	0.988	3.47	0.06	0.984	1.65	0.07	0.968	2.29	0.07	0.942	5.01	0.05
16	0.984	4.91	0.06	0.986	3.40	0.02	0.980	2.01	0.10	0.970	1.86	0.07	0.974	7.27	0.13
17	0.984	1.11	0.10	0.987	3.22	0.08	0.982	1.30	0.27	0.982	0.18	0.32	0.894	4.32	0.12
18	0.985	0.65	0.02	0.983	1.26	0.01	0.979	1.34	0.23	0.982	0.91	0.26	0.985	0.51	0.26
19	0.983	3.08	0.20	0.983	3.66	0.13	0.978	1.14	0.12	0.983	1.47	0.23	0.936	5.12	0.19
20	0.985	1.61	0.04	0.986	2.41	0.17	0.983	1.07	0.19	0.973	3.11	0.30	0.939	5.03	0.20
μ	**0.987**	**4.27**	**0.16**	**0.985**	**4.86**	**0.13**	**0.980**	**1.60**	**0.15**	**0.975**	**3.33**	**0.17**	**0.944**	**4.56**	**0.13**
σ	**0.003**	**4.20**	**0.19**	**0.010**	**3.49**	**0.13**	**0.004**	**1.17**	**0.12**	**0.007**	**2.33**	**0.14**	**0.036**	**2.98**	**0.10**

The bold values signify the average and standard deviations for the registration accuracy and are of importance while evaluating the overall efficacy of the proposed method.

Table 3
Comparison of registration accuracies in terms of 95% HD and timing requirements for NLTPS-UNI, NLTPS-CORR and NLTPS-REGCORR, TPS (Rohr et al., 2001) and B-splines (Rueckert et al., 1999) registration methods. μ signifies the mean values and σ the standard deviation. A low HD value corresponds to good contour registration accuracy.

P#	NLTPS-UNI		NLTPS-CORR		NLTPS-REGCORR		TPS	(Rohr et al., 2001)	B-splines		(Rueckert et al., 1999)
	Time (s)	HD (mm)	Time (s)	HD (mm)	Time (s)	HD (mm)	Time (s)	HD (mm)	Grid	Time (s)	HD (mm)
1	92.15	1.51	87.62	3.13	87.58	1.89	50.15	1.84	12×20	147.32	9.35
2	72.21	0.78	67.78	0.78	67.93	1.07	22.71	2.32	13×15	98.30	1.07
3	122.02	1.47	115.19	1.64	115.05	1.74	83.91	2.09	15×20	126.30	2.08
4	123.66	0.82	116.91	0.94	109.70	1.30	94.58	1.40	17×19	140.47	1.07
5	111.06	1.07	105.54	0.82	105.73	1.30	55.35	2.35	14×19	107.82	8.06
6	99.08	0.82	93.81	0.82	93.46	1.98	47.20	2.32	14×18	89.98	6.16
7	175.63	1.10	166.81	1.56	171.96	1.64	153.14	2.61	18×22	146.59	5.04
8	129.14	0.73	123.68	1.07	125.78	1.56	96.95	2.96	17×20	192.83	3.38
9	138.08	2.56	130.89	2.23	134.11	2.86	99.88	2.39	17×20	218.27	4.93
10	131.82	1.04	130.90	1.04	124.41	1.30	89.56	1.98	18×19	214.63	5.98
11	124.86	0.94	124.21	0.94	122.08	2.14	65.33	2.22	15×19	146.87	3.03
12	115.77	0.94	115.59	1.47	123.65	1.64	85.82	5.00	17×19	163.02	4.60
13	132.74	1.30	130.64	1.30	125.23	1.30	84.02	1.84	16×20	141.72	4.83
14	106.81	1.04	122.51	1.04	99.38	1.04	57.14	0.82	14×19	100.61	6.50
15	112.38	1.07	105.28	1.10	105.48	1.30	70.43	2.22	16×18	110.42	6.06
16	106.42	1.74	98.15	1.40	112.74	1.51	62.91	2.71	15×19	209.27	2.90
17	90.26	1.10	84.55	0.73	84.30	1.30	44.14	1.04	15×16	73.57	7.18
18	125.64	1.30	119.38	1.56	118.90	1.82	72.02	1.64	17×18	195.15	2.32
19	158.11	2.86	149.98	2.32	150.53	2.56	126.19	1.66	19×20	135.03	7.01
20	101.42	1.10	95.34	1.16	97.42	1.30	62.99	2.08	16×18	186.74	5.51
μ	**118.46**	**1.31**	**114.24**	**1.35**	**113.77**	**1.63**	**76.22**	**2.17**	–	**147.25**	**4.85**
σ	**23.54**	**0.57**	**23.05**	**0.61**	**23.43**	**0.48**	**29.79**	**0.85**	–	**43.81**	**2.30**

The bold values signify the average and standard deviations for the registration accuracy and are of importance while evaluating the overall efficacy of the proposed method.

4.4. Registration of non mid-gland slices

The proposed registration method has been evaluated with one axial mid-gland slice for each of the 20 patients. However, 2D sweeps of the prostate from base to apex/mid-gland in TRUS are available for two patients 6 and 7 respectively. Therefore, to validate the proposed registration method for non mid-gland slices the afore-mentioned patient datasets are used. Since a tracking system is not used with the TRUS probe, the probe angle cannot be retrieved; that obviates an assumption in the validation process that the TRUS slices are parallel to the corresponding MR slices. A total of nine axial slices are taken for patient 6 and 7 axial slices for patient 7 respectively. Table 5 shows the slice-by-slice registration accuracies for the patients 6 and 7 in terms of DSC, TRE and TLE. Fig. 14 shows the TRUS-MR slices from base to apex for patient 6 and their qualitative registration results.

Table 6 summarizes the different experiments performed for mid-gland/non mid-gland registrations with manual/automatic segmentation on different patient cohorts.

4.5. Statistical analysis

4.5.1. Control points

It is observed from Table 7 for a varied number of control points (M1, M2 and M3) and for the proposed with 13 control points (NLTPS-REGCORR) that the average DSC values are almost similar.
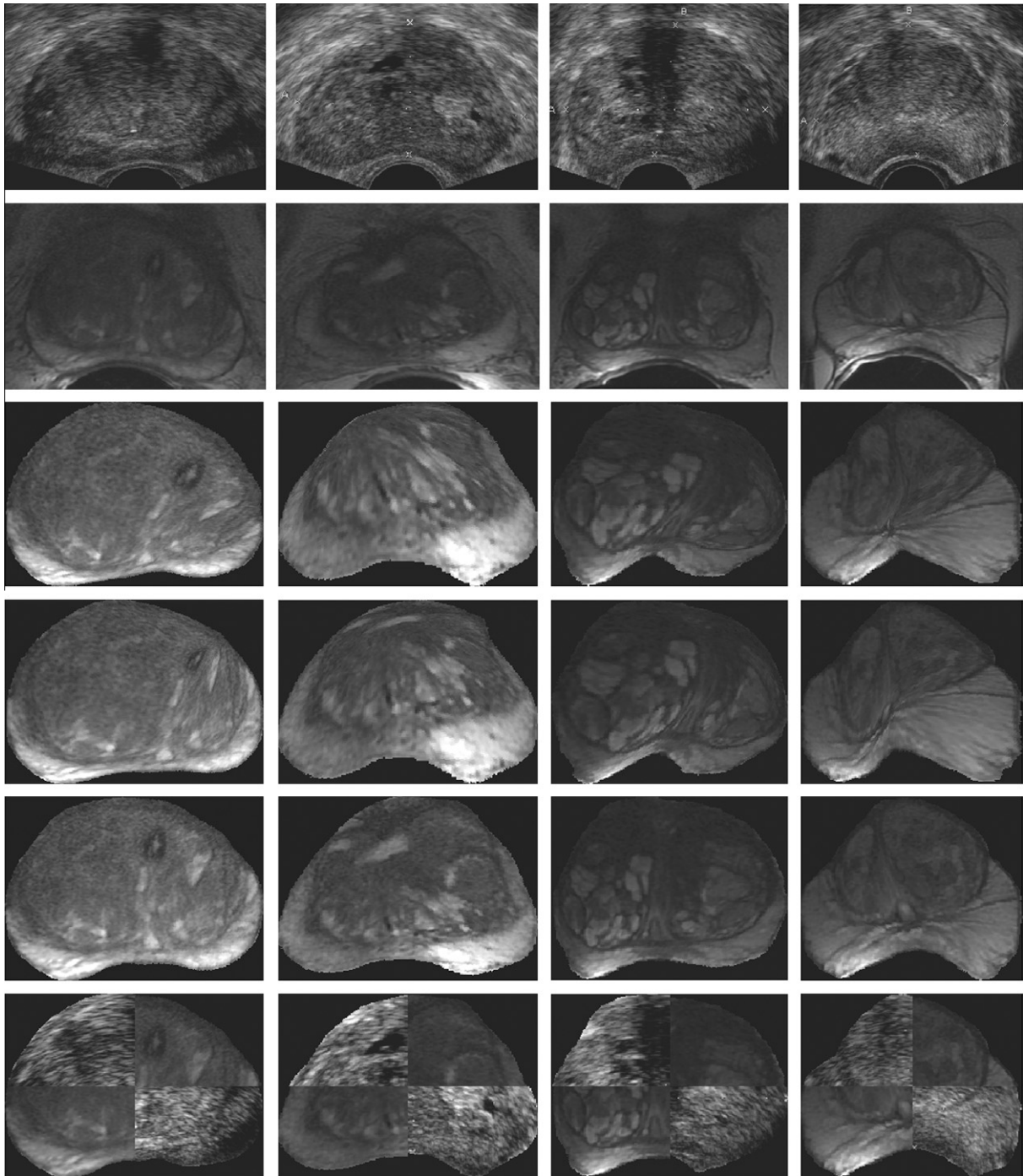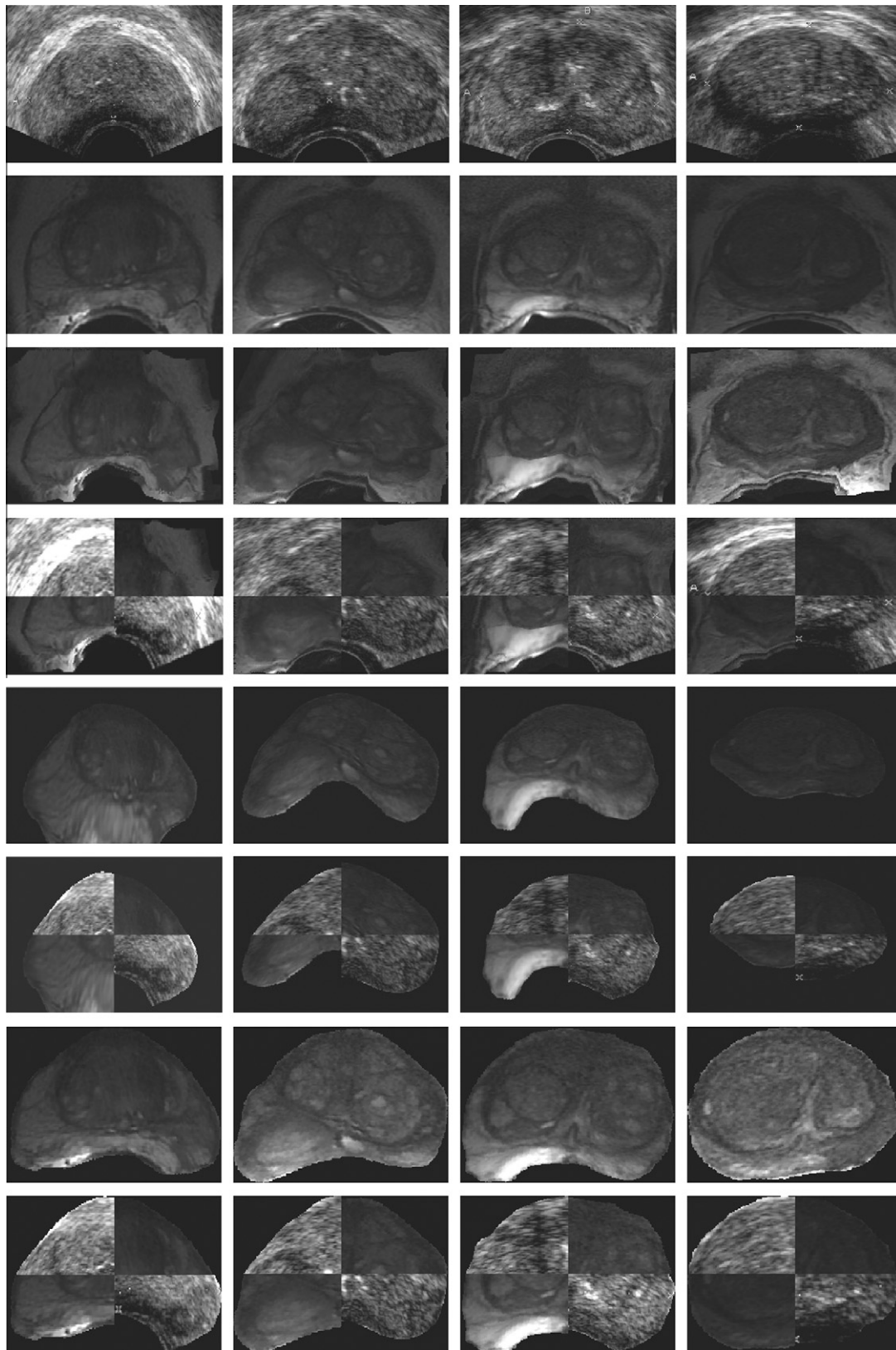
Fig. 11. Qualitative registration results of NLTPS-UNI, NLTPS-CORR and NLTPS-REGCORR for patients 7, 8, 11 and 12. Rows 1 and 2 are the fixed TRUS and the moving MR images respectively. Rows 3 and 4 show the transformed MR images for the methods NLTPS-UNI and NLTPS-CORR respectively. Rows 5 and 6 show the transformed MR images and the checker-board of the fixed TRUS and the transformed MR images for the method NLTPS-REGCORR (proposed).

Therefore, to measure the statistical significance of the null hypothesis that the mean values of all the methods are similar we need to verify the normality and homogeneity of the variances (homoscedasticity) of the data (Sokal and Rohlf, 1995; Zar, 1999). Common data transformations such as log, square-root and arcsine transformations could not suitably scale the data to a normal distribution. Hence, Lilliefors test (Lilliefors, 1967) was used on the raw data to verify the normality of the distribution. The test rejected the null hypothesis of normal distribution. Consequently, Levene's test (Levene, 1960) is used to verify the homogeneity of

the variances for the three methods which accepted the null hypothesis (Levene's test is used to measure the homogeneity of variances if the data are non-normal, otherwise, Bartlett's test could have been used). Since the measurements of DSC are taken for the same samples over the methods (M1, M2, M3 and NLTPS-REGCORR), we considered Friedman's test (Friedman, 1939) (similar to two-way ANOVA) for paired data. The test accepted the null hypothesis that the mean ranks for the DSC of the four methods with different sets of control points are similar with $\chi^2 = 3.45$, $d.f = 3$, $p < 0.03$.

Fig. 12. Qualitative registration results for TPS, B-splines compared with the proposed method (NLTPS-REGCORR). The columns signify patient cases 1, 5, 15 and 17 respectively. Rows 1 and 2 show the fixed TRUS and moving MR images respectively. Rows 3 and 4 show the transformed MR and checkerboard using traditional TPS. Similarly, rows 5 and 6 show the results of B-splines and rows 7 and 8 show the results of the proposed method.

The TRE values in Tables 1 and 2 respectively do not follow a normal distribution. However, the log transformation of the raw data accepted the null hypothesis of normality of the data using Lilliefors test. The null hypothesis of the homoscedasticity of variances for the log-transformed data is also true when Bartlett's test (Bartlett, 1937) is used. A one-way ANOVA (Analysis of Variance)
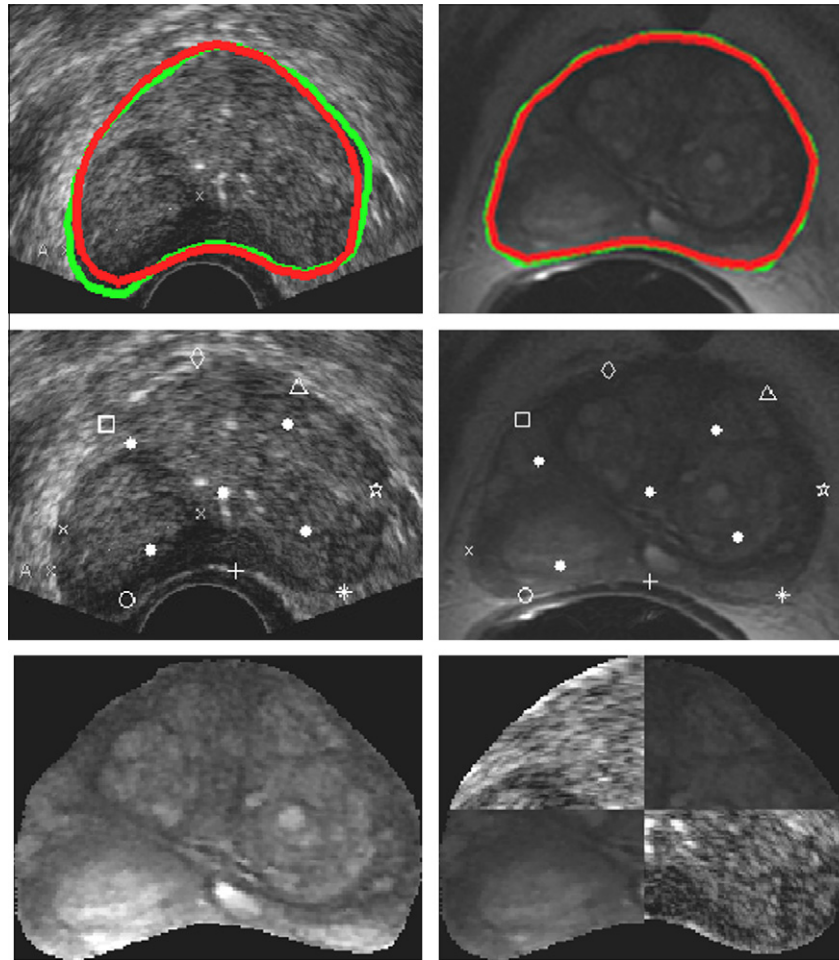
Fig. 13. Qualitative registration results with point correspondences established according to automatically segmented prostate contours. The first row shows the contours obtained using automatic segmentation method (in red) and manual segmentation (in green) on both TRUS and MR images. The second row shows the point correspondences on the prostate for both the TRUS and MR images and the third row shows the resulting fused TRUS-MR image and the TRUS-MR checker-board. (For interpretation of the references to colour in this figure legend, the reader is referred to the web version of this article.)

Table 4

Quantitative global and local registration accuracies when automatic segmentation (Ghose et al., 2011a) method is used. μ denotes the mean and σ denotes the standard deviation of the respective measures. A high DSC, low HD, low TRE and low TLE represent good registration accuracy.

P#	DSC	HD (mm)	TRE (mm)	TLE (mm)
5	0.986	0.78	1.28	0.09
6	0.981	1.30	0.90	0.02
7	0.985	1.30	2.27	0.06
8	0.983	1.56	1.40	0.07
9	0.982	1.56	1.58	0.23
10	0.987	1.10	1.65	0.04
11	0.977	1.66	1.60	0.05
12	0.983	1.40	2.03	0.22
13	0.981	1.30	3.04	0.12
14	0.979	1.40	1.67	0.04
μ	**0.982**	**1.34**	**1.74**	**0.09**
σ	**0.003**	**0.25**	**0.59**	**0.07**

The bold values signify the average and standard deviations for the registration accuracy and are of importance while evaluating the overall efficacy of the proposed method.

Table 5

Slice-by-slice registration accuracies for base to apex slices. μ denotes the mean and σ denotes the standard deviation of the respective measures. S# denotes slice number from base to apex. A high DSC, low TRE and low TLE represent good registration accuracy.

S#	Patient 6			Patient 7		
	DSC	TRE (mm)	TLE (mm)	DSC	TRE (mm)	TLE (mm)
1	0.961	1.39	0.12	0.978	1.73	0.06
2	0.974	1.26	0.09	0.985	2.69	0.03
3	0.981	0.70	0.02	0.981	0.95	0.02
4	0.977	1.66	0.21	0.980	2.20	0.08
5	0.974	0.73	0.03	0.974	2.80	0.56
6	0.973	0.29	0.01	0.976	3.21	0.23
7	0.972	1.09	0.54	0.984	3.57	0.19
8	0.980	0.95	0.25	–	–	–
9	0.982	1.08	0.08	–	–	–
μ	**0.975**	**1.02**	**0.15**	**0.980**	**2.45**	**0.17**
σ	**0.006**	**0.41**	**0.17**	**0.004**	**0.90**	**0.19**

The bold values signify the average and standard deviations for the registration accuracy and are of importance while evaluating the overall efficacy of the proposed method.

(Fisher, 1932) is used to test the null hypothesis of similarity of means where the null hypothesis is accepted at 95% confidence level with $F = 5.08$, $d.f = 3$, $p = 0.0035$. Although, the ANOVA test accepted the null hypothesis, a Dunn's post test (Dunn,

1964) is additionally performed to identify the dissimilarities in the TRE means of the methods M1, M2, M3 and NLTPS-REGCORR. The pairwise comparison test revealed that only M3 and NLTPS-REGCORR TRE means are siginifically different with $p < 0.05$.
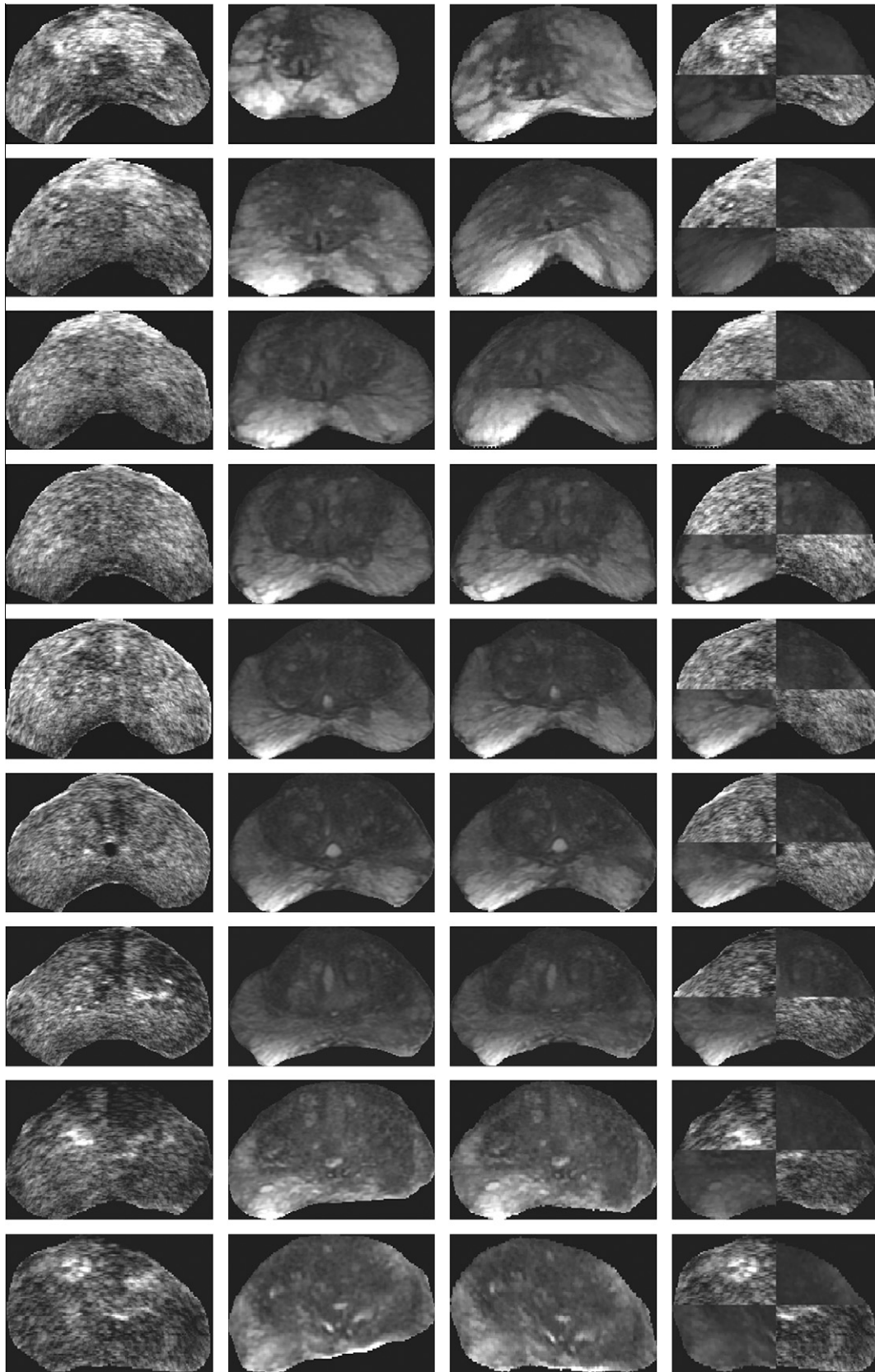
Fig. 14. Qualitative results of the proposed method when applied to non mid-gland slice. The rows show the base to apex slice registrations (rescaled) top-to-bottom for Patient 6.

Fig. 15 shows the mean estimates of the TRE with their confidence intervals for the given methods. The figure depicts that the mean

TRE of the proposed NLTPS-REGCORR is significantly different than M3 method (proposed method with no internal points).

Table 6
Quantitative registration results for mid-gland and off mid-gland registration with manual or automatic segmentation on different patient cohorts.

Exp#	1	2	3
Method	NLTPS-REGCORR	NLTPS-REGCORR	NLTPS-REGCORR
Segmentation	Manual	Manual	Automatic
Prostate	Mid-gland	Off mid-gland	Mid-gland
Patients	1–20	6, 7	5–14
DSC	0.980 ± 0.004	0.977 ± 0.006	0.982 ± 0.003
TRE (mm)	1.60 ± 1.17	1.64 ± 0.97	1.74 ± 0.59

4.5.2. Registration methods

It is observed from Table 7 that the DSC and HD values for all the three methods (NLTPS-UNI, NLTPS-CORR and NLTPS-REGCORR) are similar. Therefore, a statistical analysis of the mean DSC and HD values is done separately for the afore-mentioned method leaving out TPS (Rohr et al., 2001) and the B-splines (Rueckert et al., 1999) registration methods. Common data transformations could not scale the given DSC values of Table 2 into a normal distribution and hence, Lilliefors test used to verify the normality of the distribution rejected the null hypothesis. Consequently, Levene's test is used to verify the homogeneity of the variances for the three methods which accepted the null hypothesis. Since the measurements of DSC of Table 2 and HD of Table 3 are taken for the same samples over the methods (NLTPS-UNI, NLTPS-CORR and NLTPS-REGCORR), we used Friedman's test for paired data. The test rejected the null hypothesis that the mean ranks for the DSC and HD and values of the 3 methods are similar with $\chi^2 = 25.27$, $d.f = 2$, $p < 0.0001$ and $\chi^2 = 17.29$, $d.f = 2$, $p < 0.0001$ respectively. This signifies that at least one of the three methods differs in mean rank from the rest. Therefore, Dunn's post test is used for pairwise comparison between the methods to identify the dissimilarity. The test identified that the means of the DSC values for NLTPS-UNI and NLTPS-CORR are not statistically significantly different and those for NLTPS-UNI & NLTPS-REGCORR and NLTPS-CORR & NLTPS-REGCORR are statistically significantly different with $p < 0.001$ for both respectively. Similar statistical significances are observed for the means of HD values for the first three methods of Table 3.

Analyzing the TRE columns of Table 2 it is observed that a log transformation of the raw data could suitably scale the data into a normal distribution. Therefore, Bartlett's test is used to analyze the homoscedasticity of the variances that accepted the null hypothesis. The data sample sizes being different for the five methods (19 values for NLTPS-UNI & NLTPS-CORR and 20 values for the remaining methods), the Kruskal–Wallis test (non-parametric one-way ANOVA)(Kruskal and Wallis, 1952) is used to compare the means of the ranked log-transformed TRE values. The test rejected the hypothesis of equality of ranked means with $\chi^2 = 19.6$, $d.f = 4$, $p = 0.0006$, which signifies that at least one of the method has statistically significantly different mean TRE than the remaining. Consequently, the Dunn's post test is performed to find the dissimilarity in the mean ranks of the TRE values. The test revealed that NLTPS-REGCORR (proposed method) has a statistically significantly different mean TRE than NLTPS-CORR and the B-splines registration methods with $p < 0.005$, while not so significantly different than NLTPS-UNI and TPS registration methods. Nevertheless, the analysis of raw data for the TRE columns in Table 2 show a 2–3 times improvement in mean TRE for the proposed method than NLTPS-UNI and TPS. The TLE value of 0.15 ± 0.12 mm for NLTPS-REGCORR signifies a low repeatability error in identification of the anatomical targets by clinical experts. Fig. 16 shows the box-plot obtained from the Kruskal–Wallis test for the ranked TRE values of the 5 registration methods. Fig. 17 shows the pairwise comparisons of log-transformed TRE values for the different methods. The figure reveals that NLTPS-REGCORR has statistically significantly different mean TRE than NLTPS-CORR and B-splines.

On analysis of the DSC data in Table 2 and HD data in Table 3 for NLTPS-REGCORR, TPS and B-Splines respectively, it is observed that the data do not follow a normal distribution and the data are heteroscedastic. Therefore, none of the classical statistical hypothesis testing method can be applied to compare the means of the DSC and HD measures of the proposed method to that of the TPS and B-splines. However, the mean DSC and HD values of the proposed method are better than the TPS and B-splines methods.

4.5.3. Automatic segmentation

The DSC values of Table 4 and the DSC values for patients 5–14 related to NLTPS-REGCORR in Table 2 follow a normal distribution with homogeneity of variances. Therefore, a two-tailed Student's t-test (Gosset, 1908) is used to identify the similarity of the means of the DSC data for the proposed method with manual segmentation and the proposed method with automatic segmentation. The null hypothesis is accepted with $p < 0.01$ signifying that the mean DSC value obtained when automatic segmentation is employed is similar to that obtained with manual segmentation. However, for the HD values of the same set of patients as shown in Tables 4 and 3 (HD column of NLTPS-REGCORR) need to be square-root transformed to be scaled into a normal distribution. Thereafter,

Table 7
A comparison of the global and local registration accuracies for the different methods and their statistical significance. The methods are abbreviated from A to H for M1, M2, M3, NLTPS-UNI, NLTPS-CORR, NLTPS-REGCORR, TPS and B-splines respectively. HD and TRE are in (mm) with μ denoting the mean and σ the standard deviation. Statistical significance is computed for 95% confidence interval i.e a $p < 0.05$ is considered as similarity of means with high statistical significance, while a very low p-value denotes significantly different means. The letters within brackets in the p-value field (p) denote the methods that are used for comparison. The empty p-value fields signify that either the comparisons are irrelevant or could not be computed due to non-normal and heteroscedastic data.

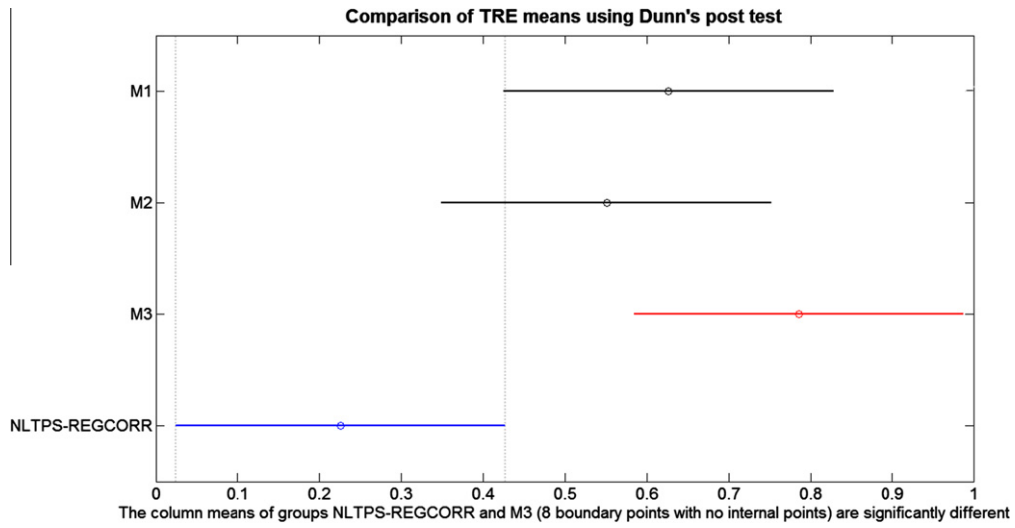| Methods		M1	M2	M3	NLTPS-UNI	NLTPS-CORR	NLTPS-REGCORR	TPS (Rohr et al., 2001)	B-splines (Rueckert et al., 1999)
Abbrv.		A	B	C	D	E	F	G	H
DSC	μ	0.981	0.981	0.981	0.987	0.985	0.980	0.975	0.944
	σ	0.004	0.006	0.005	0.003	0.010	0.004	0.007	0.036
	p	< 0.03 (A,B,C,F)	–	–	< 0.01 (D,F)	< 0.01 (E,F)	< 0.0001 (D,E,F)	–	–
HD	μ	–	–	–	1.31	1.35	1.63	2.17	4.85
	σ	–	–	–	0.57	0.61	0.48	0.85	2.30
	p	–	–	–	< 0.01 (D,F)	< 0.01 (E,F)	< 0.0001 (D,E,F)	–	–
TRE	μ	2.73	2.55	3.34	4.27	4.86	1.60	3.33	4.56
	σ	3.01	2.98	4.16	4.20	3.49	1.17	2.33	2.98
	p	$=0.0035$ (A,B,C,F)	–	< 0.05 (C,F)	–	–	< 0.005 (E,F,H)	–	< 0.0006 (D–H)

Fig. 15. TRE means for different methods with significant difference between M3 (red line) and NLTPS-REGCORR (blue line). (For interpretation of the references to colour in this figure legend, the reader is referred to the web version of this article.)
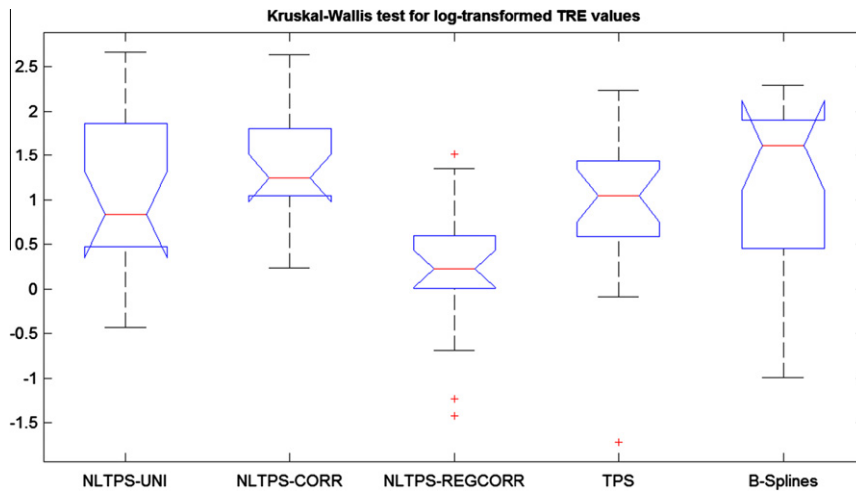

Fig. 16. Kruskal–Wallis comparison of medians of ranked TRE values. Non-overlapping notches signify that the median values for the given methods are significantly different at 95% confidence level.
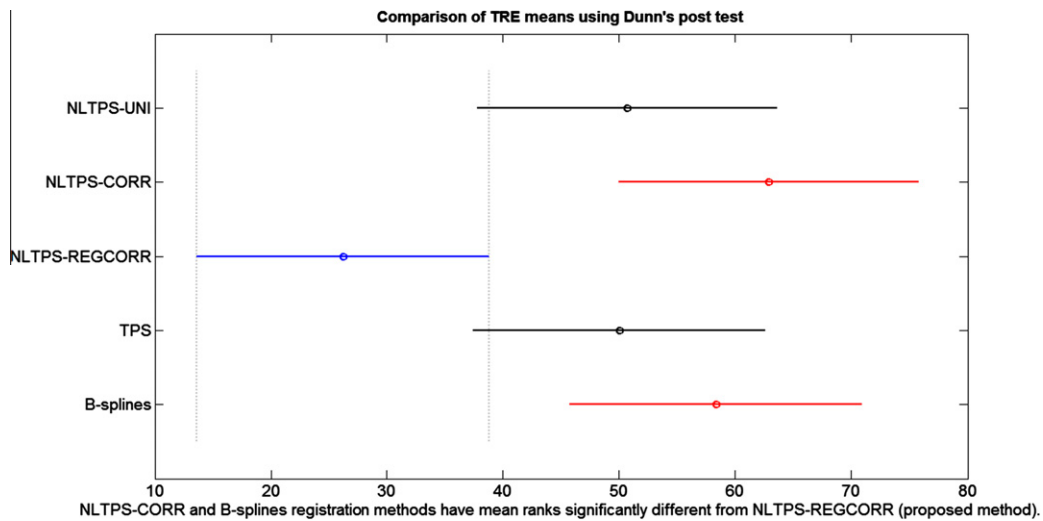

Fig. 17. TRE means for different methods with significant difference between NLTPS-REGCORR (blue line) and NLTPS-CORR and B-splines (red lines). (For interpretation of the references to colour in this figure legend, the reader is referred to the web version of this article.)

the homoscedasticity of the data is determined and a two-tailed Student's t-test revealed statistically significant similar mean HD values with $p < 0.01$.

The log-transformed TRE data of Table 4 and those from TRE column of NLTPS-REGCORR for patients 5–14 of Table 2 show a normal distribution but heterogeneity of variances. Therefore, a two-tailed Welch's t-test (Welch, 1947) is performed that accepted the null hypothesis signifying that the means of the log-transformed TRE of the methods compared are statistically significantly similar with $p < 0.01$.

5. Discussions

The statistical analysis in Section 4.5.1 of the DSC data in Table 1 for the methods with different sets of control points reveal that the mean DSC values for all the three methods and the proposed NLTPS-REGCORR in Table 2 are similar. However, the mean TRE of M3 (eight boundary points with no internal points) is significantly lower than the proposed method. This suggests that internal points are necessary to maintain clinically acceptable deformations of the prostate gland (as seen in Fig. 10). Although methods M1 (six boundary and four internal points) and M2 (10 boundary and six internal points) do not show statistically significantly different mean TRE values than NLTPS-REGCORR, the values are definitely higher than the proposed method that signify inaccurate local deformations.

The analysis in Section 4.5.2 of the data in Tables 2 and 3 allow us to infer that the region overlap measures (DSC and HD) are slightly better for the methods NLTPS-UNI and NLTPS-CORR and inferior for traditional TPS and B-splines methods than those of NLTPS-REGCORR. However, the TRE values are low for the proposed method with high statistical significance when compared with NLTPS-CORR and B-splines registration methods. Although, the TRE values of TPS and NLTPS-UNI are not statistically significantly different than the proposed method, they are definitely $2 - 3$ times higher than NLTPS-REGCPRR. This signifies that the local deformations of the prostate gland anatomical structures (targets) are clinically acceptable as provided by the method NLTPS-REGCORR. The transformed MR images obtained as the results of the methods NLTPS-UNI and NLTPS-CORR (rows 3 and 4 of Fig. 11) clearly illustrate the fact that the transformation of the gland anatomical structures are not acceptable for clinical procedures and may be verified quantitatively from the TRE value columns of NLTPS-UNI and NLTPS-CORR in Table 2 for the respective patients.

The possible reason for slightly improved region overlap measures with NLTPS-UNI and NLTPS-CORR than the proposed NLTPS-REGCORR is that the non-linear TPS equations aim at minimizing the image differences of the TRUS and MR binary mask images. Therefore, the prostate boundaries are well aligned for NLTPS-UNI and NLTPS-CORR. On the contrary, NLTPS-REGCORR constrains the non-linear transformations with the additional term of regularized bending energy and correspondence localization errors. This results in smooth and clinically meaningful gray-level deformations of the gland anatomical structures in addition to a satisfactory prostate overlap of the transformed MR image with that of the TRUS. The global overlap measures shown in Tables 2 and 3 when compared to those of the proposed method apparently indicate that our proposed method provides better prostate gland overlap than B-splines, although not significantly better than traditional TPS.

Considering the TRE measure to be more appropriate in evaluating registration accuracy, our method provides the least mean TRE with less than 3 mm (as suggested by the clinical experts) accuracy when compared to the traditional spline-based methods

or the variations of the proposed method. Patient cases 1, 5, 15 and 17 of Fig. 12 (columns 1–3 and 5–6) reveal that the B-spline transformation (rows 5–6) has significantly distorted the prostate gland, which are also reflected in the TRE values of the respective patient rows of Table 2. Although traditional TPS transformation (rows 3–4) does not show any significant deformation of the prostate other than rugged transformations around the prostate edges as shown in Fig. 12, the TRE values for the respective patients are higher than the proposed method as seen from Table 2. Therefore, the proposed method seems to provide better registration accuracies when compared with the other methods.

The analysis of the global and local registration accuracies in Table 4 and in Table 2 for patients 5–14 shows that automatic segmentation does not significantly affect the registration accuracies compared to when manual segmentation is used. The example shown in Fig. 13 also shows that there are significant overlaps between the manually and automatically segmented contours both in TRUS and MR images. Finally, the validation of the proposed registration method on the base and non mid-gland slices (Table 6) have shown high registration accuracies with < 3 mm average TRE for patients 6 and 7 respectively.

The average times required for the methods NLTPS-CORR and NLTPS-REGCORR are similar (see Table 3). However, the average time is slightly higher for NLTPS-UNI considering 16 control points being used instead of 13 control points as in NLTPS-REGCORR. The complexity for the algorithms NLTPS-REGCORR and its variations (NLTPS-UNI and NLTPS-CORR) is $O(N + M)$, where, N and M are the number of foreground pixels for the fixed and the moving images respectively. The traditional TPS has the least average computation time, since the complexity $O(n)$ involves only the number of correspondences (n) across the fixed and moving images. However, it is to be noted that the implementation does not guarantee bijectivity of the TPS transformation and therefore suffers from distorted transformations in some cases e.g. patients 5 and 15 (columns 2 and 5, rows 3 and 4 respectively). The B-splines method requires the maximum time for registration owing to evaluation of the image similarity measure (NMI) and following a multiresolution framework for 3 resolutions. Despite the use of a multiresolution framework, the traditional B-splines fail to provide good registration accuracy in most cases. On the contrary, our proposed method does not follow any multiresolution framework; however, by the virtue of the non-linear polynomial functions, a smooth and bijective transformation is achieved. The computation time of the proposed algorithm being highly dependent on the number of image pixels can be parallelized and considering its unoptimized implementation in MATLAB, a speed-up of computation time is possible by C++/GPU programming.

6. Conclusions

A new non-linear diffeomorphic framework with TPS being the underlying transformation has been proposed to register prostate multimodal images. A method to establish point correspondences on a pair of TRUS and MR images has also been proposed that is based on the computation of Bhattacharyya distance for shape-context representations of contour points. The bijectivity of the diffeomorphism is maintained by integrating over a set of non-linear functions for both the fixed and transformed moving images. The regularized bending energy and the localization errors of the point correspondences established between the fixed and moving images have further been added to the system of non-linear equations added to the TPS constraints. This additional constraint ensured regularized deformations of the local anatomical structures inside the prostate that are meaningful for clinical interventions like prostate biopsy. The performance of the proposed method

has been compared against two variations of non-linear TPS transformations where the control points had been uniformly placed on a grid for the first and the control points were established using the proposed point correspondence method for the latter. Both these methods did not involve the regularization and only relied on the non-linear transformation functions. The results obtained on real patient datasets concluded that the overall performance of proposed method in terms of global and local registration accuracies are better compared to the two variations as well as traditional TPS and B-splines based deformable registration methods, and therefore could be feasibly applied for prostate biopsy procedures. The proposed method has been validated against varied number of control points that inferred that control points inside the prostate gland are necessary to maintain clinically meaningful deformations and that 8 boundary points capturing the inflexions of the prostate curve are optimally suitable than less or more boundary control points. The proposed method has been shown to be not affected by automatic segmentation inaccuracies owing to the robustness of the automatic segmentation method employed. Validation of the registration method on the base and non mid-gland slices have shown high global and local registration accuracies illustrating the robustness of the method.

The proposed non-linear TPS framework with regularization may be applied to 3D prostate volume registration. However, a slice-by-slice point correspondences may be established after resampling the prostate volumes. The TRUS-MR slice correspondences chosen manually in our experiment can also be chosen automatically with the use of an EM tracker attached to the TRUS probe that will provide the spatial position of the TRUS slice in a pre-acquired prostate TRUS/MR volume during the needle-biopsy. An automatic method based on information theory and statistical shape analysis to find the MR slice that closely corresponds to the TRUS axial slice is currently under investigation. The algorithm can be parallelized if programmed on GPU and therefore may be useful for real-time multimodal fusion of prostate images during biopsy.

Acknowledgments

References

Alterovitz, R., Goldberg, K., Kurhanewicz, J., Pouliot, J., Hsu, I.C., 2004. Image registration for prostate MR spectroscopy using biomechanical modeling and optimization of force and stiffness parameters. In: Proc. of 26th Annual Int. Conf. of the IEEE Engineering in Medicine and Biology Society (EMBS), San Francisco, CA, USA.

Andriole, G.L., Crawford, E.D., Grubb, R.L., Buys, S.S., Chia, D., Church, T.R., Fouad, M.N., Gelmann, E.P., Reding, D.J., Weissfeld, J.L., Yokochi, L.A., O'Brien, B., Clapp, J.D., Rathmell, J.M., Riley, T.L., Hayes, R.B., Kramer, B.S., Izmirlian, G., Miller, A.B., Pinsky, P.F., Prorok, P.C., Gohagan, J.K., Berg, C.D., 2009. Mortality results from a randomized prostate-cancer screening trial. The New England Journal of Medicine 360, 1310–1319.

Avants, B.B., Epstein, C.L., Grossman, M., Gee, J.C., 2008. Symmetric diffeomorphic image registration with cross-correlation: evaluating automated labeling of elderly and neurodegenerative brain. Medical Image Analysis 12, 26–41.

Bartlett, M.S., 1937. Properties of sufficiency and statistical tests. Proceedings of the Royal Society of London, Series A: Mathematical and Physical Sciences 160, 268–282.

Baumann, M., Mozer, P., Daanen, V., Troccaz, J., 2009. Prostate biopsy assistance system with gland deformation estimation for enhanced precision. In: Proc. of MICCAI, September, pp. 57–64.

Baumann, M., Mozer, P., Daanen, V., Troccaz, J., 2012. Prostate biopsy tracking with deformation estimation. Medical Image Analysis 16, 562–576.

Belongie, S., Malik, J., Puzicha, J., 2002. Shape matching and object recognition using shape contexts. IEEE Transactions on Pattern Analysis and Machine Intelligence 24, 509–522.

Besl, P., McKay, N., 1992. A method for registration of 3D shapes. IEEE Transactions on Pattern and Machine Intelligence (PAMI) 14, 239–256.

Bhattacharyya, A., 1943. On a measure of divergence between two statistical populations defined by their probability distribution. Bulletin of the Calcutta Mathematical Society 35, 99–110.

Bogers, H.A., Sedelaar, J.P., Beerlage, H.P., de la Rosette, J.J., Debruyne, F.M., Wijkstra, H., Aarnink, R.G., 1999. Contrast-enhanced three-dimensional power Doppler angiography of the human prostate: correlation with biopsy outcome. Urology 54, 97–104.

du Bois d'Aische, A., Craene, M.D., Haker, S., Weisenfeld, N., Tempany, C., Macq, B., Warfield, S.K., 2004. Improved non-rigid registration of prostate MRI. In: Proc. of MICCAI, Rennes, France, pp. 845–852.

Bookstein, F., 1991. Morphometric Tools for Landmark Data: Geometry and Biology. Cambridge University Press, Cambridge, UK.

Carroll, P., Shinohara, K., 2010. Transrectal Ultrasound Guided Prostate Biopsy. Technical Report, Department of Urology, University of California, San Francisco. http://urology.ucsf.edu/patientGuides.html (accessed 30.12.10).

Chen, T., Kim, S., Zhou, J., Metaxas, D., Rajagopal, G., Yue, N., 2009. 3D meshless prostate segmentation and registration in image guided radiotherapy. In: Proc. of MICCAI, London, UK, pp. 43–50.

Cheung, M.R., Krishnan, K., 2009. Interactive deformation registration of endorectal prostate MRI using ITK thin plate splines. Academic Radiology 16, 351–357.

Chrisochoides, N., Fedorov, A., Kot, A., Archip, N., Black, P., Clatz, O., Golby, A., Kikinis, R.,Warfield, S.K., 2006. Toward real-time image guided neurosurgery using distributed and grid computing. In: Proc. ACM/IEEE Conference on Supercomputing (SC 2006), p. 37.

Cool, D.W., Bax, J., Romagnoli, C., Ward, A.D., Gardi, L., Karnik, V., Izawa, J., Chin, J., Fenster, A., 2011. Fusion of MRI to 3D TRUS for mechanically-assisted targeted prostate biopsy: system design and initial clinical experience. In: Proc. of MICCAI Workshop on Prostate Cancer Imaging, Computer Aided Diagnosis, Prognosis and Intervention, pp. 121–133.

Daanen, V., Gastaldo, J., Giraud, J.Y., Fourneret, P., Descotes, J.L., Bolla, M., Collomb, D., Troccaz, J., 2006. MRI/TRUS data fusion for brachytherapy. International Journal of Medical Robotics 2, 256–261.

Davatzikos, C., 1997. Spatial transformation and registration of brain images using elastically deformable models. Computer Vision and Image Understanding 66, 207–222.

Dice, L.R., 1945. Measures of the amount of ecologic association between species. Ecology 26, 297–302.

Domokos, C., Nemeth, J., Kato, Z., 2012. Nonlinear shape registration without correspondences. IEEE Transactions on Pattern Analysis and Machine Intelligence 34, 943–958.

Dunn, O.J., 1964. Multiple comparisons using rank sums. Technometrics 6, 241–252.

Fei, B.W., Kemper, C., Wilson, D.L., 2003. A comparative study of warping and rigid body registration for the prostate and pelvic MR volumes. Computerized Medical Imaging and Graphics 27, 267–281.

Fisher, R.A., 1932. Statistical Methods for Research Workers. Oliver & Boyd, Edinburgh and London.

Friedman, M., 1939. A correction: the use of ranks to avoid the assumption of normality implicit in the analysis of variance. Journal of American Statistical Association 34, 109.

Ghose, S., Oliver, A., Martí, R., Lladó, X., Freixenet, J., Mitra, J., Vilanova, J.C., Comet, J., Meriaudeau, F., 2011a. Multiple mean models of statistical shape and probability priors for automatic prostate segmentation. In: Proc. of MICCAI Workshop on Prostate Cancer Imaging, Computer Aided Diagnosis, Prognosis and Intervention, pp. 35–46.

Ghose, S., Oliver, A., Martí, R., Lladó, X., Freixenet, J., Vilanova, J., Meriaudeau, F., 2010. Prostate segmentation with texture enhanced active appearance model. In: Proc. IEEE International Conference on Signal-Image Technology & Internet-Based Systems, pp. 18–22.

Ghose, S., Oliver, A., Martí, R., Lladó, X., Freixenet, J., Vilanova, J., Meriaudeau, F., 2011b. A probabilistic framework for automatic prostate segmentation with a statistical model of shape and appearance. In: Proc. IEEE International Conference on Image Processing, pp. 725–728.

Gosset, W.S., 1908. The probable error of a mean. Biometrika 6, 1–25.

Hu, Y., Ahmed, H.U., Taylor, Z., Allem, C., Emberton, M., Hawkes, D., Barratt, D., 2012. MR to ultrasound registration for image-guided prostate interventions. Medical Image Analysis 16, 687–703.

Huttenlocher, D.P., Klanderman, G.A., Rucklidge, W.J., 1993. Comparing images using the Hausdorff distance. IEEE Transaction in Pattern Analysis and Machine Intelligence 15, 850–863.

Jonker, R., Volgenant, A., 1987. A shortest augmenting path algorithm for dense and sparse linear assignment problems. Computing 38, 325–340.

Kadoury, S., Yan, P., Xu, S., Glossop, N., Choyke, P., Turkbey, B., Pinto, P., Wood, B.J., Kruecker, J., 2010. Realtime TRUS/MRI fusion targeted-biopsy for prostate cancer: a clinical demonstration of increased positive biopsy rates. In: Proc. of MICCAI Workshop on Prostate Cancer Imaging, Computer Aided Diagnosis, Prognosis and Intervention, pp. 52–62.

Kaplan, I., Oldenburg, N.E., Meskell, P., Blake, M., Church, P., Holupka, E.J., 2002. Real time MRI-ultrasound image guided stereotactic prostate biopsy. Magnetic Resonance Imaging 20, 295–299.

Karnik, V.V., Fenster, A., Bax, J., Cool, D.W., Gardi, L., Gyacskov, I., Romagnoli, C., Ward, A.D., 2010. Assessment of image registration accuracy in three-dimensional transrectal ultrasound guided prostate biopsy. Medical Physics 37, 802–813.

de Koning, H.J., Auvinen, A., Sanchez, A.B., et al., 2002. Large-scale randomized prostate cancer screening trials: program performances in the european randomized screening for prostate cancer trial and the prostate, lung, colorectal and ovary cancer trial. International Journal of Cancer 97, 237–244.

Kroon, D.J., 2008. B-spline grid, image and point based registration. <http://www.mathworks.com/matlabcentral/fileexchange/20057>.

Kruskal, W.H., Wallis, W.A., 1952. Use of ranks in one-criterion variance analysis. Journal of the American Statistical Association 47, 583–621.

Levene, H., 1960. Robust tests for equality of variances. In: Contributions to Probability and Statistics, I. Olkin ed. Stanford University Press, Palo Alto, California.

Lilliefors, H.W., 1967. On the Kolmogorov–Smirnov test for normality with mean and variance unknown. Journal of American Statistical Association 62, 399–402.

Lu, J., Srikanchana, R., McClain, M., Wang, Y., Xuan, J., Sesterhenn, I.A., Freedman, M.T., Mun, S.K., 2000. A statistical volumetric model for characterization and visualization of prostate cancer. In: Proc. of SPIE, pp. 142–153.

Marquardt, D.W., 1963. An algorithm for least-squares estimation of nonlinear parameters. SIAM Journal on Applied Mathematics 11, 434–441.

Maurer, C.R., Fitzpatrick, J.M., Wang, M.Y., Member, S., Galloway, R.L., Maciunas, R.J., Allen, G.S., 1997. Registration of head volume images using implantable fiducial markers. IEEE Transactions on Medical Imaging 16, 447–462.

Maurer, C.R., McCrory, J.J., Fitzpatrick, J.M., 1993. Estimation of accuracy in localizing externally attached markers in multimodal volume head images. Proceedings of SPIE Medical Imaging 1898, 43–54.

Mitra, J., Martí, R., Oliver, A., Lladó, X., Ghose, S., Vilanova, J.C., Meriaudeau, F., 2012. Prostate multimodality image registration based on B-splines and quadrature local energy. International Journal of Computer Assisted Radiology and Surgery 7, 445–454.

Mitra, J., Oliver, A., Martí, R., Lladó, X., Vilanova, J.C., Meriaudeau, F., 2010. Multimodal prostate registration using thin-plate splines from automatic correspondences. In: Proc. of Intl. Conference on Digital Image Computing:Techniques and Applications (DICTA'10), Sydney, Australia, pp. 587–592.

Mitra, J., Srikantha, A., Sidibé, D., Martí, R., Oliver, A., Lladó, X., Vilanova, J.C., Meriaudeau, F., 2012. A shape-based statistical method to retrieve 2D TRUS-MR slice correspondence for prostate biopsy. In: Proc. of SPIE Medical Imaging, San Diego, Calfornia, USA, pp. 83143M-1–9.

Mizowaki, T., Cohen, G.N., Fung, A.Y.C., Zaider, M., 2002. Towards integrating functional imaging in the treatment of prostate cancer with radiation: the registration of the MR spectroscopy imaging to ultrasound/CT images and its implementation in treatment planning. International Journal of Radiation Oncology Biology Physics 54, 1558–1564.

Narayanan, R., Kurhanewicz, J., Shinohara, K., Crawford, E.D., Simoneau, A., Suri, J.S., 2009. MRI-ultrasound registration for targeted prostate biopsy. In: Proc. of IEEE Intl. Symposium on Biomedical Imaging: From Nano to Macro (ISBI'2009), Boston, MA, pp. 991–994.

Natarajan, S., Marks, L.S., Margolis, D.J., Huang, J., Macairan, M.L., Lieu, P., Fenster, A., 2011. Clinical application of a 3D ultrasound-guided prostate biopsy system. Urologic Oncology 29, 334–342, Seminar Article.

Nemeth, J., Domokos, C., Kato, Z., 2009a. Nonlinear registration of binary shapes. In: Proc. IEEE International Conference on Image Processing (ICIP'09), Cairo, Egypt, pp. 1001–1004.

Nemeth, J., Domokos, C., Kato, Z., 2009b. Recovering planar homographies between 2D shapes. In: Proc. IEEE International Conference on Computer Vision (ICCV'09), Kyoto, Japan, pp. 2170–2176.

Oguro, S., Tokuda, J., Elhawary, H., Haker, S., Kikinis, R., Tempany, C.M., Hata, N., 2009. MRI signal intensity based B-spline nonrigid registration for pre- and intraoperative imaging during prostate brachytherapy. Magnetic Resonance Imaging 30, 1052–1058.

Ourselin, S., Roche, A., Prima, S., Ayache, N., 2000. Block matching: a general framework to improve robustness of rigid registration of medical images. In: Medical Image Computing and Computer-Assisted Intervention (MICCAI 2000). Lecture Notes in Computer Science, vol. 1935, pp. CH373–CH373.

Papadimitriou, C., Stieglitz, K., 1982. Combinatorial Optimization: Algorithms and Complexity. Prentice Hall.

Porter, C.R., O'Donnell, C., Crawford, E.D., Gamito, E.J., Kim, J., Tewari, A., 2010. Predicting the Outcome of the Random Prostate Biopsy. Technical Report, Department of Urology, State University of New York, Stony Brook, NY. <Http://www.cancernews.com/data/Article/230.asp> (accessed 07.06.10).

Reynier, C., Troccaz, J., Fourneret, P., Dusserre, A., Gay-Jeune, C., Descotes, J.L., Bolla, M., Giraud, J.Y., 2004. MRI/TRUS data fusion for prostate brachytherapy: preliminary results. Medical Physics 31, 1568–1575.

Rohr, K., Stiehl, H.S., Sprengel, R., Buzug, T.M., Weese, J., Kuhn, M.H., 2001. Landmark-based elastic registration using approximating thin-plate splines. IEEE Transactions on Pattern Analysis and Machine Intelligence 20, 526–534.

Roobol, M.J., Schroder, F.H., 2003. European randomized study of screening for prostate cancer: achievements and presentation. BJU International 92, 117–122.

Rueckert, D., Sonoda, L.I., Hayes, C., Hill, D.L.G., Leach, M.O., Hawkes, D.J., 1999. Nonrigid registration using free-form deformations: application to breast MR images. IEEE Transactions on Medical Imaging 18, 712–721.

Shen, D.G., Herskovits, E., Davatzikos, C., 2001. An adaptive focus statistical shape model for segmentation and shape modeling of 3d brain structures. IEEE Transactions on Medical Imaging 20, 257–271.

Singh, A.K., Kruecker, J., Xu, S., Glossop, N., Guion, P., Ullman, K., Choyke, P.L., Wood, B.J., 2008. Initial clinical experience with real-time transrectal ultrasonography-magnetic resonance imaging fusion-guided prostate biopsy. British Journal of Urology International 101, 841–845.

Sokal, R.R., Rohlf, F.J., 1995. Biometry: The Principles and Practice of Statistics in Biological Research, third ed. W.H. Freeman, New York.

Szeliski, R., Lavallée, S., 1996. Matching 3-D anatomical surfaces with non-rigid deformations using octree-splines. International Journal of Computer Vision 18, 171–196.

Veltman, J., Goossen, T., Laguna, P., Wijkstra, H., de la Rosette, J., 2002. New technical improvements for TRUS in the diagnosis of prostate cancer. European Urology Supplements 1, 8–14.

Vilanova, J.C., Barceló-Vidal, C., Comet, J., Boada, M., Barceló, J., Ferrer, J., Albanell, J., 2011. Usefulness of prebiopsy multi-functional and morphologic MRI combined with the free-to-total PSA ratio in the detection of prostate cancer. American Journal of Roentgenology 196, W715–W722.

Vishwanath, S., Bloch, B.N., Rosen, M., Chappelow, J., Toth, R., Rofsky, N., Lenkinski, R., Genega, E., Kalyanpur, A., Madabhushi, A., 2009. Integrating structural and functional imaging for computer assisted detection of prostate cancer on multi-protocol In Vivo 3 Tesla MRI. In: Proceedings of SPIE 7260, pp. 726031.1–12.

Welch, B.L., 1947. The generalization of 'students' problem when several different population varlances are involved. Biometrika 34, 28–35.

Xiao, G., Bloch, B., Chappelow, J., Genega, E., Rofsky, N., Lenkinski, R., Madabhushi, A., 2010. A structural-functional MRI-based disease atlas:application to computer-aided-diagnosis of prostate cancer. In: Proc. of SPIE Medical Imaging:Image Processing, February, pp. 762303.1–12.

Xu, S., Kruecker, J., Turkbey, B., Glossop, N., Singh, A.K., Choyke, P., Pinto, P., Wood, B.J., 2008. Real-time MRI-TRUS fusion for guidance of targeted prostate biopsies. Computer Aided Surgery 13, 255–264.

Zar, J.H., 1999. Biostatistical Analysis, fourth ed. Prentice Hall, Upper Saddle River, NJ.

Zhu, Y., Williams, S., Zwiggelaar, R., 2006. Computer technology in detection and staging of prostate carcinoma: a review. Medical Image Analysis 10, 178–199.